

RESEARCH ARTICLE

10.1002/2013JA019574

Key Points:

- Propagation of shock-induced aurora tracked with meridian scanning photometers
- Auroral propagation timing performed for electron and proton precipitation
- Two-pulse proton shock aurora onset observed in some but not all locations

Correspondence to:

J. M. Holmes,
jeffrey.holmes@kirtland.af.mil

Citation:

Holmes, J. M., M. G. Johnsen, C. S. Deehr, X.-Y. Zhou, and D. A. Lorentzen (2014), Circumpolar ground-based optical measurements of proton and electron shock aurora, *J. Geophys. Res. Space Physics*, 119, 3895–3914, doi:10.1002/2013JA019574.

Received 12 NOV 2013

Accepted 16 APR 2014

Accepted article online 23 APR 2014

Published online 14 MAY 2014

Corrected 28 JUL 2014

This article was corrected on 28 JUL 2014. See the end of the full text for details.

Circumpolar ground-based optical measurements of proton and electron shock aurora

J. M. Holmes^{1,2}, M. G. Johnsen^{3,4}, C. S. Deehr⁵, X.-Y. Zhou⁶, and D. A. Lorentzen^{1,7}

¹Arctic Geophysics, University Centre in Svalbard, Longyearbyen, Norway, ²Now at Space Vehicles Directorate, Air Force Research Laboratory, Kirtland AFB, New Mexico, USA, ³Department of Physics and Technology, University of Tromsø, Tromsø, Norway, ⁴Now at Tromsø Geophysical Observatory, University of Tromsø, Tromsø, Norway, ⁵Geophysical Institute, University of Alaska Fairbanks, Fairbanks, Alaska, USA, ⁶Institute of Geophysics and Planetary Physics, University of California, California, USA, ⁷Birkeland Centre for Space Science, Bergen, Norway

Abstract Meridian scanning photometer (MSP) data are combined with global ultraviolet images from the Polar Ultraviolet Imager instrument to estimate the timing and propagation speed of shock auroras previously studied using solely space-based ultraviolet auroral imagery. The multispectral nature of the MSPs, including the presence of a Balmer beta channel, enables the discrimination between proton and electron aurora. Following a near-magnetic noon onset, the occurrence of auroral emissions created by shocked precipitating protons and electrons is observed to propagate tailward, along the auroral oval with speeds of several km/s, consistent with the shock propagation speed in the solar wind. In two cases, shock aurora propagation speeds along the auroral oval determined from satellite imagery are confirmed, to within calculated uncertainties, with ground-based timing. The majority of instruments detect low-energy discrete auroral arcs poleward of diffuse, higher-energy aurora. Evidence of a previously reported two-pulse proton aurora shock onset is detected at some, but not all, locations.

1. Introduction

While it is well known that the interplanetary magnetic field (IMF) embedded in the solar wind exhibits significant control over the Earth's magnetosphere, the solar wind ram pressure, P_{ram} (also known as dynamic pressure), is increasingly found to play a role over its configuration, size, and shape [e.g., Boudouridis *et al.*, 2003; Liou *et al.*, 2007; Laundal and Østgaard, 2008]. It follows that such influence over the magnetospheric configuration will have a corresponding impact on the size and location of the auroral ovals, polar caps, and the associated intensity of aurora, polar electric fields, Birkeland currents, and ionospheric convection [Boudouridis *et al.*, 2007, and references therein].

Auroras observed right after the impingement of a sudden increase in solar wind ram pressure (e.g., pressure pulses or interplanetary shocks) exhibit interesting features that are different from both typical auroral activity on the dayside and nightside. Often referred to as “shock aurora,” this sudden intensification is often observed initially near magnetic noon. However, this is dependent on the shock front orientation. Oblique shocks, with high inclinations in the GSM X-Y plane, have been observed to produce auroral brightening closest in magnetic local time (MLT) to the initial shock tangent area with the bow shock [e.g., Tsurutani *et al.*, 2001a; Fuselier *et al.*, 2004; Kozlovsky *et al.*, 2005].

As the solar wind pressure enhancement propagates past Earth, shock auroras are observed in many cases as tailward propagating enhancements along the dawnside and duskside of the auroral oval, often reaching the magnetic midnight sector after several minutes. The shock auroral propagation speed, when mapped from the auroral oval to the magnetospheric equatorial plane, is thought to agree with the speed of the shock along the magnetopause. However, there are some reports of near-instantaneous (~1–2 min or less) auroral enhancement over part of [Chua *et al.*, 2001] or the entire auroral oval [Zesta *et al.*, 2000; Boudouridis *et al.*, 2003; Meurant *et al.*, 2003]. The differences between the reported fast and slowly propagating disturbances are ascribed to fast Alfvén waves propagating across magnetic flux tubes and speeds typical of the shock in the magnetosheath, respectively [e.g., Kozlovsky *et al.*, 2007]. There is a body of evidence suggesting that the state of the IMF both before (referred to as magnetospheric “preconditioning”) and after the shock impingement upon the magnetosphere also has a significant effect [Boudouridis *et al.*, 2003; Echer *et al.*, 2011].

There appears to be no single physical magnetospheric generation mechanism for shock auroras. As a broader category, they are discussed as a sudden enhancement in brightness coincident with a solar wind shock passage (or equivalently in terms of the sudden change in their particle and flux characteristics detected in situ). Since this enhancement maps to different magnetospheric regions as it propagates along the auroral oval (e.g., cusp, low-latitude boundary layer (LLBL) and/or boundary or central plasma sheet (BPS/CPS) on the dayside, then BPS/CPS along the magnetospheric flanks), it is natural to expect different generation mechanisms giving rise to different auroral morphologies. During the shock passage, compression of the dayside magnetosphere is thought to generate shock auroras by way of a combination of processes, e.g., betatron acceleration, magnetic merging, reductions in the mirror ratio, loss cone instability owing to adiabatic compression, viscous interactions, magnetic shearing, Alfvén wave generation, Birkeland current enhancement, and so on. Such possible mechanisms are discussed in detail by *Zhou and Tsurutani* [1999], *Tsurutani et al.* [2001a], *Liou et al.* [2002, 2007], *Laundal and Østgaard* [2008], *Motoba et al.* [2009], and *Zhou et al.* [2003, 2009].

The vast majority of recent studies of shock or pressure pulse-induced magnetospheric, ionospheric, and auroral dynamics have been made with space-based UV-observing systems such as Dynamics Explorer 1 and 2, Polar Ultraviolet Imager (UVI), International Monitor for Auroral Geomagnetic Effects (IMAGE) FUV, Thermosphere, Ionosphere, Mesosphere Energetics and Dynamics Global Ultraviolet Imager, and Defense Meteorological Satellite Program Special Sensor Ultraviolet Spectrographic Imager [e.g., *Craven et al.*, 1986; *Sitar et al.*, 1998; *Spann et al.*, 1998; *Zhou and Tsurutani*, 1999; *Brittnacher et al.*, 2000; *Chua et al.*, 2001; *Vorobjev et al.*, 2001; *Zhang et al.*, 2003, 2008; *Meurant et al.*, 2003, 2004; *Zhou et al.*, 2003; *Liou et al.*, 2007; *Su et al.*, 2011; *Yang et al.*, 2011]. Some results of relevance to the current study include propagation speeds of shock auroral luminosity between 6 and 11 km s⁻¹ along the auroral oval [*Zhou and Tsurutani*, 1999], the identification of two distinct particle energy populations giving rise to diffuse aurora within the auroral oval and discrete arcs along its poleward edge [*Tsurutani et al.*, 2001b; *Zhou et al.*, 2003, 2009], evidence of morphological differences, such as propagation speed and location, between electron- and proton-created shock aurora [*Meurant et al.*, 2003], and asymmetry of shock auroral enhancement about the noon-midnight axis being more pronounced during negative IMF B_z periods [*Meurant et al.*, 2004].

While the above studies using space-based auroral imaging benefit by being able not only to view the entire auroral oval but also, in some cases, to make estimates of precipitated energy flux, average energy [e.g., *Chua et al.*, 2001] and total hemispheric power [e.g., *Meurant et al.*, 2004], they are often limited by the relatively coarse spatial and temporal resolution of such instruments. Cases where ground-based data are included take advantage of typically higher spatial and temporal resolution, and also the ability of ground-based measurements to resolve spatiotemporal ambiguity inherent in measures of particles and electromagnetic fields by satellites. Since the sunward side of the magnetosphere is further compressed during impulsive shock or high-pressure events, ground-based studies have generally focused on dayside measurements [e.g., *Vorobjev*, 1977; *Sandholt et al.*, 1994, 1998; *Lorentzen and Moen*, 2000; *Kozlovsky et al.*, 2005; *Motoba et al.*, 2009; *Zhou et al.*, 2009; *Liu et al.*, 2011]. Exceptions are specific to geomagnetic storm times, studies considering influence of P_{ram} with respect to substorms [e.g., *Lyons et al.*, 2000; *Meurant et al.*, 2005], or those that focus on high-latitude convection enhancements [e.g., *Cerisier et al.*, 2005; *Coco et al.*, 2008; *Boudouridis et al.*, 2011, and references therein].

Detailed measurements of the response of cusp aurora to changes in P_{ram} , IMF B_y , and B_z were discussed by *Sandholt et al.* [1994]. MSPs in Danmarkshavn (DMH), northeast Greenland, and Ny-Ålesund (NYA), Svalbard, observed green $\lambda 557.7$ nm and red $\lambda 630.0$ nm auroral forms in the 09–15 MLT range. Cusp auroras were observed to shift equatorward during strong, sudden pressure enhancements ($\Delta P_{ram}/P_{ram} \geq 0.5$) along with magnetic signatures of localized enhanced convection. In addition, a significant asymmetry in the drift of prenoon auroral forms was found in response to variations in IMF B_y that correlated with smaller pressure enhancements ($0.1 < \Delta P_{ram}/P_{ram} < 0.5$).

From the Southern Hemisphere, *Motoba et al.* [2009] reported observations of postnoon shock aurora (~15 MLT), combining the large-scale tailward propagation measured by the different instruments of IMAGE FUV with smaller-scale details observed by optical and magnetometer data from South Pole Station. Special attention was given to the relative occurrence of proton and electron aurora during the shock impingement. By comparing the evolution of the shock aurora observed in Doppler-shifted Lyman α ($\lambda 121.82$ nm, produced

solely by precipitating hydrogen) and OI λ 135.6 nm (produced mainly by electrons but with a contribution from protons [see Galand and Lummerzheim, 2004]), the case revealed that the preliminary shock-induced impulse (PI) of auroral brightening was attributable to mainly proton precipitation in the afternoon sector. A main impulse (MI) [Araki, 1994], composed of both proton- and electron-produced aurora, was observed shortly thereafter. This is the first ground-based detection of a two-step development of shock aurora.

Using all-sky imager (ASI) and MSP data from Ny-Ålesund, Zhou *et al.* [2009] performed a detailed morphological treatment of dayside shock auroral forms. A doubling of the cusp aurora meridional width and equatorward expansion of the equatorward boundary was also reported, indicative of low-latitude magnetopause reconnection during the shock passage. The authors conclude that the diffuse, green-dominated aurora occurs mainly on closed field lines, while the discrete red arcs poleward of that lie along the open/closed field line boundary (OCB).

In the present study, the cases presented by Zhou and Tsurutani [1999, hereafter referred to as ZT99] are revisited using ground-based MSP data from the Canadian, Greenlandic, and Scandinavian sectors, spanning a wide range in MLT. Timing of the occurrence of both proton- and electron-produced shock auroras above each ground station is used to refine the average propagation speeds on the dawnside and duskside, as previously reported. While the solar wind and shock characterization has already been performed for these cases, the UV imagery presented by ZT99 lacked the spatiotemporal resolution needed to depict the relative occurrence of proton versus electron aurora, diffuse versus discrete electron aurora, and the estimated location of the OCB.

A primary objective is to investigate whether or not increased spatiotemporal resolution, and the propagation of uncertainties in the shock auroral timing matches well with previous conclusions. If so, it reinforces the accepted notion that the ionospheric speed of the shock aurora propagation, when mapped to the magnetospheric equatorial plane, matches the speed of the shock in the solar wind. In addition, confirmation substantiates current knowledge about the various processes proposed to be responsible for shock aurora, for example, the precipitation of trapped particles on closed field lines comprising diffuse shock aurora owing to loss cone instability, reductions in the mirror ratio, and/or an enlarged loss cone.

In order to clarify the shock auroral propagation and contrast different phenomenology, the MLT range for analysis is divided into dawnside (0000–1200) and duskside (1200–2400) halves. Usage of terms with more specific relationships to magnetospheric source regions (e.g., prenoon, dayside, postdusk, nightside, predawn) is employed where appropriate. For each example, the MLT and the UT of the first shock auroral enhancement, m_0 and t_0 , respectively, are taken from spacecraft and ground magnetometer data, respectively. The MLT and UT of shock aurora arrival at station i of auroral emission wavelength j , m_{ij} and t_{ij} , respectively, are read from the MSP data.

2. Instrumentation and Data Description

2.1. Satellite Auroral Imagery

The Ultraviolet Imager (UVI) on the Polar spacecraft provided snapshots of the entire auroral oval at once and was designed to estimate characteristic parameters of auroral electrons [Torr *et al.*, 1995]. Measured auroral emissions include OI λ 130.4 nm, OI λ 135.6 nm, and two for the N₂ Lyman-Birge-Hopfield (LBH) band system: LBH short (LBHS), near λ 150 nm, and LBH long (LBHL), near λ 170 nm. Observed intensity of the LBHL channel is proportional to the auroral electron energy flux, and the intensity ratios of OI λ 135.6 nm or LBHS to LBHL can be used to infer the characteristic energy of the electron population [Strickland *et al.*, 1983; Germany *et al.*, 1994].

For the cases presented, the UVI filter sequence alternated between LBHS and LBHL, each with an 18.4 s and 36.8 s exposure. The total time of the filter cadence was 3 min and 4 s. Auroral intensities are simply presented in units of rayleigh (or derived energy flux, where appropriate), mapped to an altitude-adjusted corrected geomagnetic (AACGM) latitude (MLAT)/MLT grid [Baker and Wing, 1989]. A nominal emission altitude of 120 km is assumed for the UV emissions.

2.2. Meridian Scanning Photometers

Despite recent advances in imaging technology in the past several decades, meridian scanning photometers remain valuable instruments for high time resolution, high-sensitivity detection of auroral emissions [e.g.,

Table 1. Meridian Scanning Photometer Instrument Parameters

Site	MLAT ^a	Detector Type	Scan Method	Background	Resolution
GILL	66.3	Single PMT + filter wheel	Discrete stepping	Multi-channel	30 s, 80 bin
FSMI	67.4	Single PMT + filter wheel	Discrete stepping	Multi-channel	60 s, 17 bin
RANK	72.6	Single PMT + filter wheel	Discrete stepping	Multi-channel	60 s, 17 bin
LYR	75.2	Multiple PMT	Continuous rotation	Tilting-filter	16 s, 181 bin
NYA	76.2	Multiple PMT	Discrete stepping	None	20 s, 161 bin
DMH	77.2	Multiple PMT	Discrete stepping	None	30 s, 161 bin

^aAACGM, epoch 1995 coefficients.

[Vallance Jones et al., 1982; Sandholt et al., 2002; Lorentzen et al., 2007]. This study uses MSPs from three different research groups, whose similarities and differences are briefly outlined with instrument parameters described in Table 1. The three Canadian sector MSPs utilized in this study are currently part of the NORSTAR network: Rankin Inlet (RANK), Gillam (GILL), and Fort Smith (FSMI) [Rostoker et al., 1995]. Each instrument uses a mirror that scans the local geomagnetic meridian in an alternating fashion at elevation angles above 10°, a single photomultiplier tube (PMT), a continuously rotating filter wheel, and input optics that give a 4° field of view (FOV). They detect auroral photons through five filters: [OI] λ 630.0 nm, [OI] λ 557.7 nm, N_2^+ 1 N (0,2) λ 470.9 nm, and two near Balmer β (H_β) λ 486.1 nm that are averaged. The remaining three filters characterize the sky background. In this study, meridian scans are averaged into 17 latitude bins (80 bins for GILL), assuming emission heights of 110 km for λ 557.7 nm, λ 470.9 nm, and λ 486.1 nm and 230 km for λ 630.0 nm. Implications of the assumed altitudes are discussed in the next section. The complete scan time is 30 s, yet for RANK and FSMI, two scans are averaged together for a 1 min time resolution.

The University of Oslo operated two MSPs at Danmarkshavn and Ny-Ålesund. The angular scan range and windshield wiper-type scanning are the same as the Canadian instruments. A major difference is that the University of Oslo instruments use a dedicated photometer for each wavelength. The NYA MSP has [OI] λ 630.0 nm, [OI] λ 557.7 nm, N_2^+ 1 N (0, 1) λ 427.8 nm, and H_β λ 486.1 nm channels, while the one at DMH only detected photons at [OI] λ 630.0 nm and [OI] λ 557.7 nm. The instruments' spatial resolution is 161, 1° angular bins, with a scan time of 20 s at NYA and 30 s at DMH. No background compensation is performed for these data.

The MSP at Longyearbyen (LYR) is similar in design to the one at Poker Flat, Alaska, described in Romick [1976]. Wavelengths used in this study are identical to the instrument at NYA. This instrument is somewhat different from the others, in that it scans the geomagnetic meridian by means of a continuously rotating mirror. The scan time from horizon to horizon is 2 s. While the mirror points below the horizon, the interference filters tilt off the optical axis, resulting in a shifted, off-peak passband for each wavelength. The subsequent sky scan takes a background measurement that is subtracted from the preceding on axis, or "peak," scan. Typically, two "peak minus background" pairs are averaged for every wavelength, resulting in a 16 s overall time resolution with 181, 1° angular bins from horizon to horizon.

For the following analysis, it is important to note that precipitating protons are known to give rise to the entire spectrum of auroral emissions via processes of secondary electron generation. In contrast, electron precipitation does not produce detectable auroral hydrogen emissions [Lummerzheim et al., 2003].

3. Observations

3.1. On 10 January 1997

The period 06–11 January 1997 was declared an International Solar-Terrestrial Physics event and has been the subject of many studies with varying foci [e.g., Burlaga et al., 1998; Farrugia et al., 1998; Fox et al., 1998; Steele et al. 1998; Thomsen et al., 1998; Tsurutani et al., 1998; McEwen et al., 1999; Zesta et al., 2000; Boudouridis et al., 2005; Blagoveshchensky and Kornienko, 2007, and references therein]. However, only a handful of studies [e.g., Tsurutani et al., 1998, 2001a, 2001b; Arballo et al., 1998; Sandholt et al., 1998; Spann et al., 1998; Zhou and Tsurutani, 1999; Wüest et al., 2000, 2002] devote significant attention to the observed magnetospheric and auroral effects of the passage of the initial interplanetary (IP) shock arrival near 0100 UT, as opposed to the arrival of the magnetic cloud some hours later. The present analysis focuses exclusively on the passage of the shock across the near-Earth magnetosphere, a period of approximately 12 min.

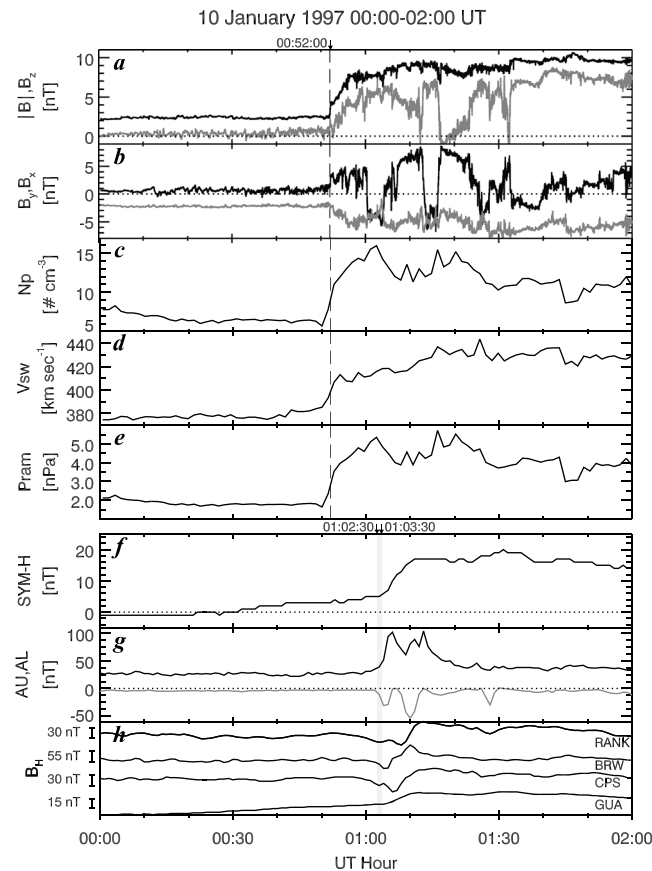


Figure 1. Solar wind parameters measured by the WIND spacecraft, and selected ground-based magnetograms and derived indices on 10 January 1997. (a) IMF magnitude (black), B_z (gray); (b) B_y GSM (black) and B_x GSM (gray); (c) solar wind proton number density; (d) bulk velocity; (e) P_{ram} ; (f) $SYM-H$ index; (g) AU (black) and AL (gray) indices; (h) horizontal-component magnetograms at Rankin Inlet (RANK, 72.6° MLAT, 1807 MLT at 0103 UT), Barrow (BRW, 70.4° MLAT, 1241 MLT at 0103 UT), Cape Schmidt (CPS, 65.1° MLAT, 1144 MLT at 0103 UT), and Guam (GUA, 9.7° MLAT, 1017 MLT at 0103 UT). The dashed, vertical black line indicates shock onset measured in situ by WIND, while the gray, vertical band indicates $t_0 \pm \sigma_{t_0}$ (see text).

[e.g., Han et al., 2007; Coco et al., 2008]. On the other hand, the increase in $SYM-H$ results primarily from the shock's compression of the dayside magnetosphere leading to an intensified and/or nearer dawn-dusk Chapman-Ferraro current.

This behavior is consistent with the examination of magnetograms from select individual stations. Also, since small AE ($\equiv AU - AL$) disturbances can be attributed to nightside activity such as pseudobreakups [Arballo et al., 1998; Zhou and Tsurutani, 2001], a comparison with other dayside magnetometers is useful. In the selection of magnetometers for analysis, an estimate is needed of the location in MLT, m_0 , of the first shock auroral enhancement. The calculated shock normal for this case is within a few degrees of the Sun-Earth line in the $X-Y$ (GSM) plane [Berdichevsky et al., 2000]. Thus, the enhancement should occur near magnetic noon. Using uncertainties in the determination of the shock normal, the location in MLT of this initial brightening is $m_0 \pm \sigma_{m_0} = 1120 \text{ MLT} \pm 20 \text{ min}$.

Figure 1h shows horizontal-component magnetograms at Barrow and Cape Schmidt, both within 1.5 h MLT of m_0 . Those data show a -20 and $+6$ nT deflection for the two stations at 0102:30–0103:30 UT, respectively. The equatorial magnetometer at Guam, slightly westward at 1020 MLT (at 0103 UT), observes an appreciable increase in its horizontal trace 2–3 min later, similar to the $SYM-H$ index.

After the first in situ detection of the solar wind shock by the SOHO spacecraft, the WIND spacecraft detected signatures of a fast forward IP shock at 0052 UT on 10 January 1997 (ZT99). At that time, it was upstream of Earth at $(85.1, -55.2, -22.1) R_E$ (GSM). Locations of WIND and other spacecraft are shown by Wüest et al. [2000]. Figure 1 shows solar wind parameters observed by WIND, indicating the arrival of the shock. The IMF magnitude increased from 2.5 to 7.5 nT, while IMF B_z increased from about 0.0 to 6.0 nT. IMF B_y and B_x became slightly more negative and positive, respectively, but remained within a few nT of 0. Proton density and solar wind speed both steeply increased, resulting in a P_{ram} ($\sim 1.16 n_p V_{sw}^2$) increase from 1.6 to 5.4 nPa over 12 min (0050–0102 UT). The mean rate of pressure increase for this period was $0.30 \text{ nPa min}^{-1}$, with $\Delta P_{ram}/P_{ram} = 2.4$.

Geomagnetic indices are shown in Figures 1f and 1g. The high-latitude indices AU and AL both show a relatively small response to the shock around 0102:30–0103:30 UT, while the equatorial $SYM-H$ index does not increase appreciably until a couple of minutes later. The deflections of the former can result from a sudden increase in precipitating particle flux, and thus increased horizontal ionospheric conductivity, associated field-aligned currents (FACs), and convection signatures from the dayside auroral zone

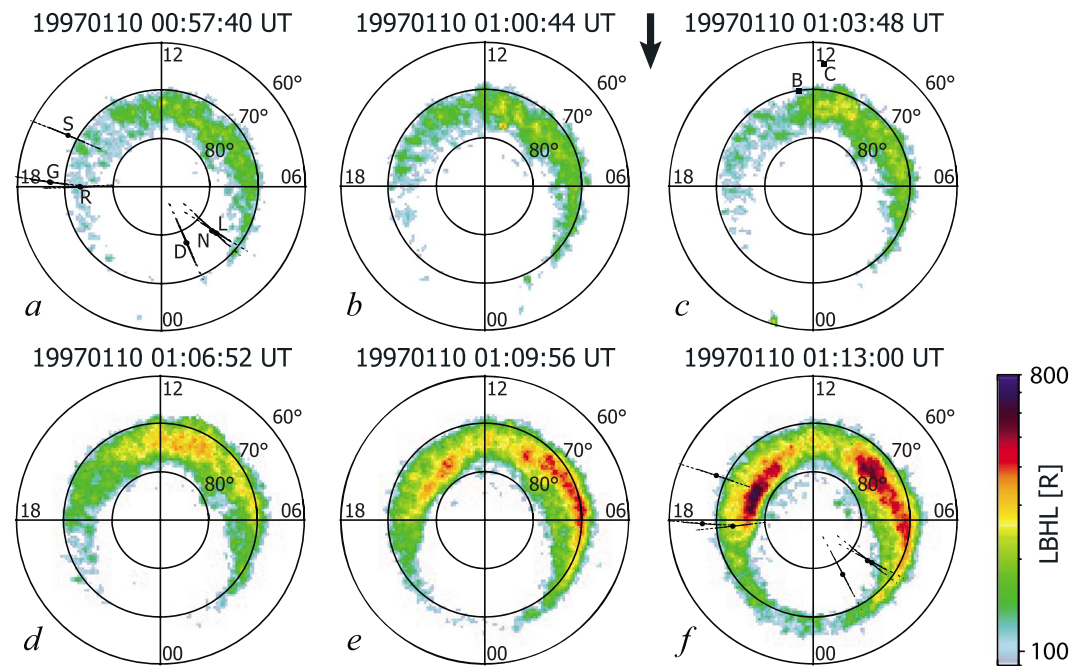


Figure 2. Propagation of shock aurora on 10 January 1997, as a sequence of Polar UVI LBHL images. A MLT/MLAT coordinate system is used, with noon at the top and dawn on the right. Mapping is done assuming a 120 km height for the emissions. The black arrow denotes the shock arrival. High-latitude magnetometers closest to the shock touchdown MLT m_0 at the shock arrival time t_0 are shown: (B) Barrow and (C) Cape Schmidt. MSP fields of view at 230 km (dotted black lines) and 110 km (solid black lines) altitude are shown at the beginning and end of the sequence for (S) Fort Smith, (G) Gillam, (R) Rankin Inlet, (D) Danmarkshavn, (N) Ny-Ålesund, and (L) Longyearbyen.

The effect of the shock impingement on the auroral oval is depicted by LBHL images from the UVI instrument in Figure 2. The first response of the auroral oval to the shock, determined by ZT99, is found to be between the 0100:44 UT and the 0103:48 UT images (Figures 2b and 2c). Their estimated shock arrival time to the magnetopause based on the shock orientation and speed was \sim 0103 UT. While the change between the two images is not drastic, difference imagery (not shown) reveals a clear enhancement, centered just before magnetic noon.

The shocked dayside aurora expands toward dawn and dusk from 0103:48 UT onward (Figure 2c), with the auroral intensity near noon approximately doubling in Figure 2d. At 0113:00 UT (Figure 2f), the shock aurora enhancement reaches the ground-based MSPs nearest to midnight (DMH, LYR, and NYA), between 0200 and 0400 MLT. By analyzing this propagation from the UVI imagery, ZT99 determine the average longitudinal propagation speed for the duskside of about \sim 6 km s⁻¹, using an average MLAT of 75°. The estimated speed for the dawnside is higher: \sim 11 km s⁻¹ along an average MLAT of 72°.

In order to determine the average speed of the shock aurora propagation between the initial brightening and detection above each MSP, we require a time t_0 of initial shock aurora occurrence, as reflected in the northern dayside auroral oval (as opposed to at the magnetopause). This is not necessarily the same time as a Sudden Commencement (SC) or Sudden Impulse (SI) [cf. Villante *et al.*, 1998], which is often identified by a sudden increase in equatorial magnetometer or geomagnetic index data.

Detailed estimators exist for determining the time delay between a transition recorded by a satellite instrument in the upstream solar wind and the dayside auroral/ionospheric response [e.g., Lockwood *et al.*, 1989, equations (1) and (6)]. For shock cases where the solar wind and ground magnetometer responses are stepwise and suitably dramatic, such responses can provide relatively accurate estimations. Since the ground-based indices and magnetograms in Figure 1 have a time resolution of 60 s, and they show an unambiguous response to the shock between 0102:30 and 0103:30 UT, we choose $t_0 = 0103:00$ UT with an uncertainty σ_{t_0} of 30 s. This also matches the longest cadence of the five MSPs, 60 s, at RANK and FSMI. In the determination of shock propagation that follows, the calculated velocities are relative to t_0 and m_0 .

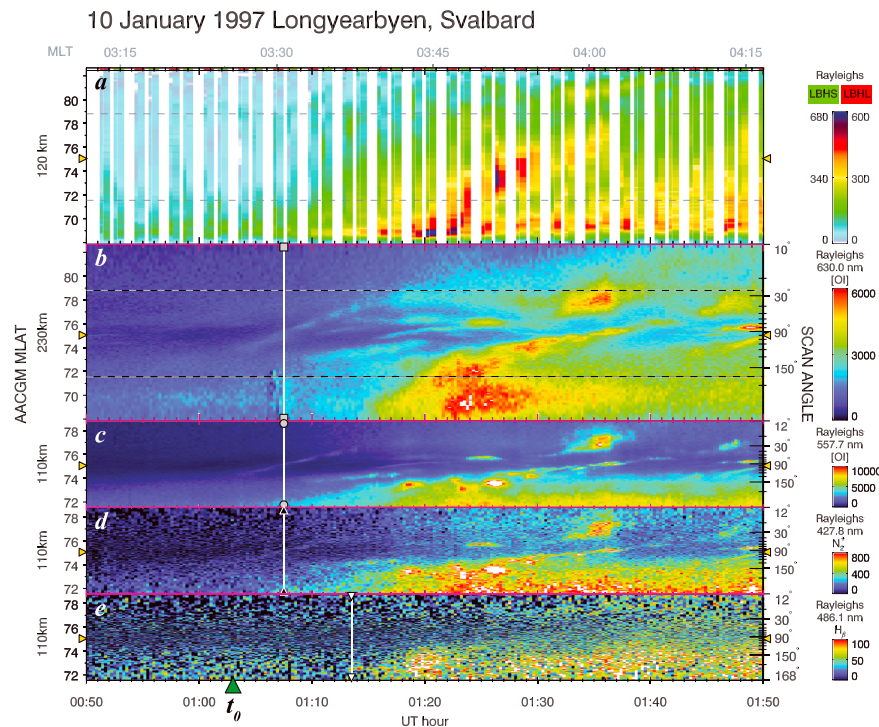


Figure 3. Polar UVI and MSP geomagnetic meridian keogram from Longyearbyen around 0330 MLT for 0050–0150 UT on 10 January 1997. Ordinate dimensions are linear in MLAT. Scan angles are indicated on the right-hand side, with minor ticks every 10° (north = 0°, south = 180°). Gold triangles indicate the station MLAT and the local geomagnetic zenith. Horizontal, dashed lines in Figures 3a and 3b demark MLAT limits for Figures 3c–3e. Emissions and mapping heights: (a) UVI LBHL, LBHS, 120 km; (b) [OI] λ 630.0 nm, 230 km; (c) [OI] λ 557.7 nm, 110 km; (d) N_2^+ 1N λ 427.8 nm, 110 km; and (e) H_β λ 486.1 nm, 110 km. Gray scale symbols connected by thin, white lines denote the shock aurora brightening for each wavelength to within 1 min ($2\sigma_{UT}$).

Figure 3a is a keogram constructed of line profiles extracted from the UVI imagery along the MSP field of view at Longyearbyen, located on the dawnside of the auroral oval between 0315 and 0415 MLT. The extraction is done following the MSP channel with the largest FOV: the λ 630.0 nm channel, assuming a 230 km emission height. Note that profiles from both LBHL and LBHS channels are present in the same keogram; different color scales are chosen to present a reasonably smooth time evolution of the shock aurora occurrence. LBHL (LBHS) extractions are identified by the green (red) rectangles atop the plot. The first signatures of the shock enhancement appear between 68 and 69° MLAT at 0110 UT in the LBHL channel.

Figures 3b–3e depict Longyearbyen MSP keogram data. For the different MSP wavelengths, an assumed altitude is chosen in order to map to MLAT and compare with the UVI extractions. For the Canadian sector MSPs, emission heights are assumed during the initial data reduction. Therefore, the same emission heights are applied to data from DMH, LYR, and NYA for consistency. Since such heights will be valid for only a narrow set of auroral altitude distributions, auroral forms with different energy and altitude distributions could be mapped to MLAT with some inaccuracy [Johnsen et al., 2012]. However, for the purposes of determining the arrival time of shock aurora over an observatory, using fixed assumed mapping heights is sufficient. This assumption holds provided the scan azimuth is roughly collinear in magnetic longitude, as is the case with these instruments.

Seconds after t_0 , a faint, discrete auroral arc appears at 130° scan angle (or \sim 74–75° MLAT) in the λ 630.0 nm, λ 557.7 nm, and λ 427.8 nm channels (Figures 3b–3d) and drifts steadily poleward over the course of about 10 min. This arc is identified as the first response of the shock onset above Svalbard [Sandholt et al., 1998], but it is not of the slowly propagating type focused on in the present analysis. Diffuse aurora at scan angles greater than about 150° appears between 0107 and 0108 UT in all channels except H_β λ 486.1 nm (Figure 3e). The arrival of this aurora does not occur in a sudden, stepwise fashion like the shock aurora near local noon [e.g., Zhou et al., 2009, Figure 4, left], but rather encroaches on the MSP meridian from the southern horizon and progresses toward zenith. This is shown in the UVI data in Figure 2 as the expansion of the auroral oval’s poleward edge.

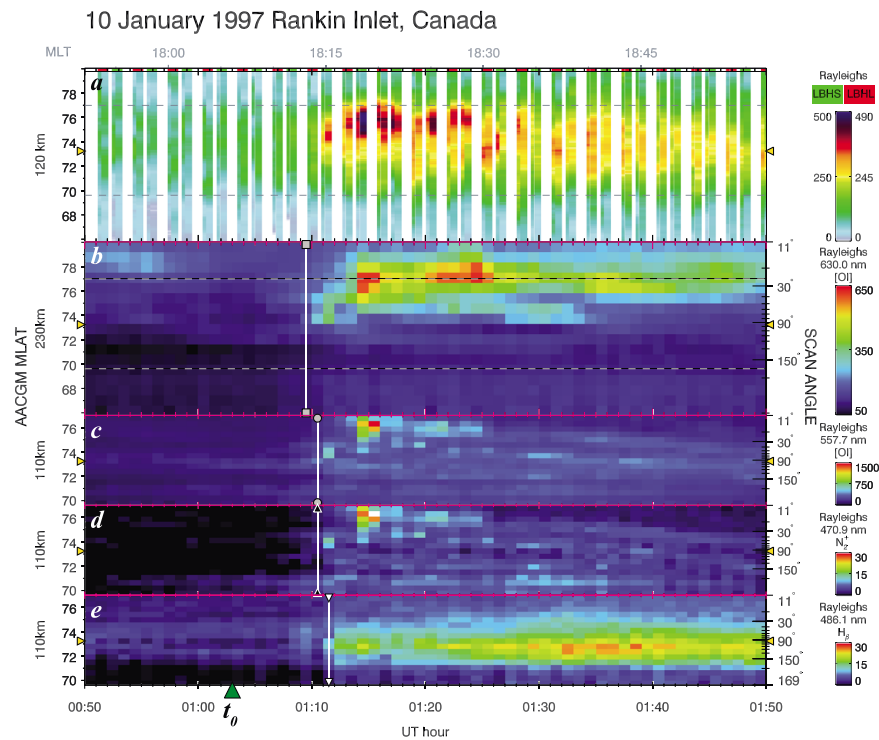


Figure 4. Polar UVI and MSP geomagnetic meridian keogram from Rankin Inlet around 1800 MLT for 0050–0150 UT on 10 January 1997. The layout is the same as Figure 3. Emissions and mapping heights: (a) UVI LBHL, LBHS, 120 km; (b) [OI] λ 630.0 nm, 230 km; (c) [OI] λ 557.7 nm, 110 km; (d) N_2^+ 1N (0, 2) λ 470.9 nm, 110 km; and (e) H_β λ 486.1 nm, 110 km.

At 0110 UT, additional discrete arcs form poleward of the diffuse emission region. The H_β λ 486.1 nm channel (λ 486.1 nm, Figure 2e) shows a subtle increase in intensity, again at scan angles greater than 150° , between 0113 and 0114 UT. Another brightening of the diffuse aurora at 0118 UT in λ 557.7 nm, λ 427.8 nm, and λ 486.1 nm (Figures 2c–2e) coincides with enhancement of the discrete electron arcs near magnetic zenith. The diffuse arcs expand poleward, reaching magnetic zenith around 0130 UT. Polar UVI images reveal these as a Sun-aligned group of arcs that are somewhat detached from the poleward edge of the predawn auroral oval, extending from about 0300 to 0600 MLT. The system also appears to be devoid of detectable proton precipitation.

On the duskside, keograms are shown for Rankin Inlet from 1750 to 1855 MLT in Figure 4. Note that Figures 2e and 2f show the shock aurora occurring at higher latitudes on the duskside (near 75° MLAT) than the dawnside. The location of the shock arrival is near or poleward of magnetic zenith for the LBH, λ 630.0 nm, λ 557.7 nm, and λ 470.9 nm emissions (Figures 4a–4d), and near or equatorward of magnetic zenith for λ 486.1 nm (Figure 4e).

The shock arrival at RANK occurred first in the λ 630.0 nm channel (Figure 4b) at 0109–0110 UT, followed by λ 557.7 nm and λ 470.9 nm 1 min later (Figures 4c and 4d). The λ 486.1 nm channel displayed a minor pulse at 0109 UT (discussed later), followed by a more pronounced pulse at 0111 UT (Figure 4e). The brightest two scans in the 10 min that follow were centered at 0114–0115 UT in all MSP channels and the UVI LBHS image at 0114:14 UT. For the period 0120–0150 UT, the LBH, λ 630.0 nm, λ 557.7 nm, and λ 470.9 nm emissions faded (Figures 4a–4d), yet proton precipitation as seen in the λ 486.1 nm channel increased through a maximum of ~ 30 R.

The separation in MLAT between the λ 630.0 nm emissions compared to λ 486.1 nm suggests that discrete electron aurora occurred poleward of diffuse proton or proton and electron aurora. This is supported by the appearance of two λ 557.7 nm auroral forms beginning at the brightening of 0114–0115 UT and drifting slowly equatorward through 0150 UT (Figure 4c). The λ 557.7 nm and λ 470.9 nm emissions at RANK covered nearly the entire meridian (Figures 4c and 4d) and decayed slightly equatorward between 0115 and 0150 UT.

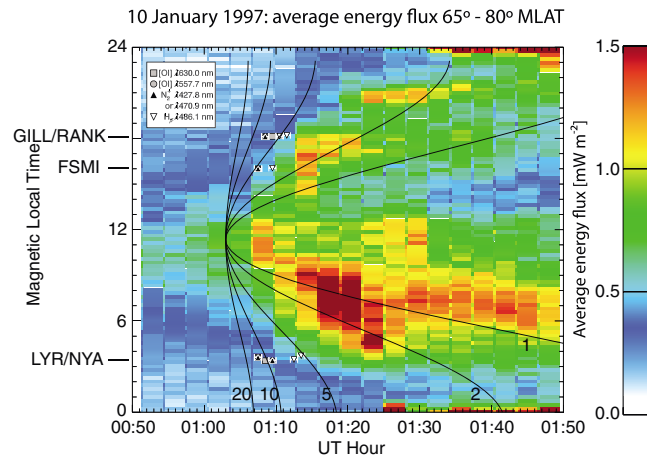


Figure 5. MLT/UT plot of average auroral energy flux between 0050 and 0150 UT and 65°–80° MLAT, derived from UVI LBHL imagery. Contours of constant speed [km s^{-1}] from (t_0, m_0) for 70.5° ($0 < \text{MLT} < 12$) and 74.0° MLAT ($12 < \text{MLT} < 24$), shown as solid black lines, represent planar shock fronts with normals parallel to the meridian connecting m_0 (1120 MLT) and the geomagnetic pole. Coordinates of shock arrival ($t_{ij} \pm \sigma_{UT}, m_{ij}$) for proton ($H\beta$, $\lambda 486.1 \text{ nm}$) and electron (N_2^+ 1N $\lambda 427.8 \text{ nm}$ or $\lambda 470.9 \text{ nm}$) emissions at each MSP are shown as white and black triangles, respectively. Emissions from metastable states [OI] $\lambda 630.0 \text{ nm}$ and [OI] $\lambda 557.7 \text{ nm}$ are shown as gray squares and circles, respectively.

and converted to electron auroral energy flux [see Strickland *et al.*, 1983; Germany *et al.*, 1994]. The bulk of precipitated electron energy flux, notably in the range 0105–0145 UT, occurred on the dawnside of the auroral oval. It should be noted that this conversion to electron energy flux neglects the contribution to the LBH bands by proton precipitation [see Galand and Lummerzheim, 2004; Knight *et al.*, 2008].

Beginning at (t_0, m_0) , contours of constant propagation speed of the shock compression effect at fixed magnetic latitudes are overlaid as solid black lines. In this visualization, the front is assumed to be planar and propagates tailward along the line containing m_0 and the geomagnetic pole. Since the shock aurora enhancement propagates along different average magnetic latitudes for the duskside and dawnside (cf. Figure 2f), the contours correspond to 70.5° MLAT for the dawnside and 74.0° MLAT for the duskside. Thus, the constant speed contours in Figure 5 appear asymmetric about m_0 . In addition, the mean shock aurora propagation latitude changes with MLT on both the dawnside and duskside; the two latitudes given above represent the average of the mean shock aurora propagation latitude between m_0 and midnight. ZT99 used 72° MLAT for the dawnside calculation but specified that it was limited to 0600–1000 MLT. Owing to the Scandinavian MSPs lying between 0200 and 0400 MLT near the time of shock aurora arrival, a lower average MLAT value is used to more accurately reflect the mean auroral oval latitude between m_0 and the MSPs (cf. Figure 2f). In the night sector between 2100 and 0300 MLT, the auroral energy flux deviated markedly from alignment with the constant speed contours, indicating the slowing of the shock propagation as the shock progressed along the magnetotail and/or the lack of effect of the passing shock on the nightside auroral configuration.

The arrival of the shock compression effect, as detected at an MSP i with wavelength j , is shown as gray scale symbols in Figure 5 and denoted t_{ij} . To illustrate the uncertainty in the t_{ij} , error bars in the abscissa are also shown, depicting coordinates as $(t_{ij} \pm \sigma_{UT}, m_{ij})$. Owing to the 60 s maximum MSP scan period, 30 s is used as σ_{UT} . The average uncertainty in MLT, $\sigma_{MLT} \sim 32 \text{ s}$, is based on both the magnetic longitudinal width of the MSP scan and also the latitudinal extent of the shock-induced auroral forms and is too small to appear in the figure. Note that if the MSP were perfectly aligned with the local geomagnetic meridian at the time of measurements, σ_{MLT} would be 0.

LYR and NYA, located very close together in MLT at about 0330, have similar t_{ij} . Combined shock propagation speeds lie in the range $9.1 \pm 4.9 \text{ km s}^{-1}$. For both of the stations, a clear time separation is observed with shock electron aurora ($\lambda 427.8 \text{ nm}$, black triangles) arriving before proton aurora ($\lambda 486.1 \text{ nm}$, white triangles). Due to a data gap, the shock arrival could not be determined with confidence in this case for DMH.

Owing to the coarse spatial resolution of this instrument and weak intensities of auroral forms after the initial shock impingement, the proportion of discrete versus diffuse aurora cannot be well distinguished and quantified. It is noteworthy to mention that the UVI imagery (not shown) shows the auroral oval near the RANK meridian to widen with the shock onset, and then become narrower with time for the period ~0110–0150 UT. With a more equatorward FOV than RANK, the GILL MSP detected only the lowest-latitude portion of the diffuse structures seen at RANK (up to ~74° MLAT with the $\lambda 630.0 \text{ nm}$ channel in Figure 4b).

A visualization of the shock aurora progression observed from the UVI instrument is combined with the observed shock arrivals for each MSP wavelength in Figure 5. UVI LBHL images have been averaged between 65°–80° MLAT, regridded in MLT and UT

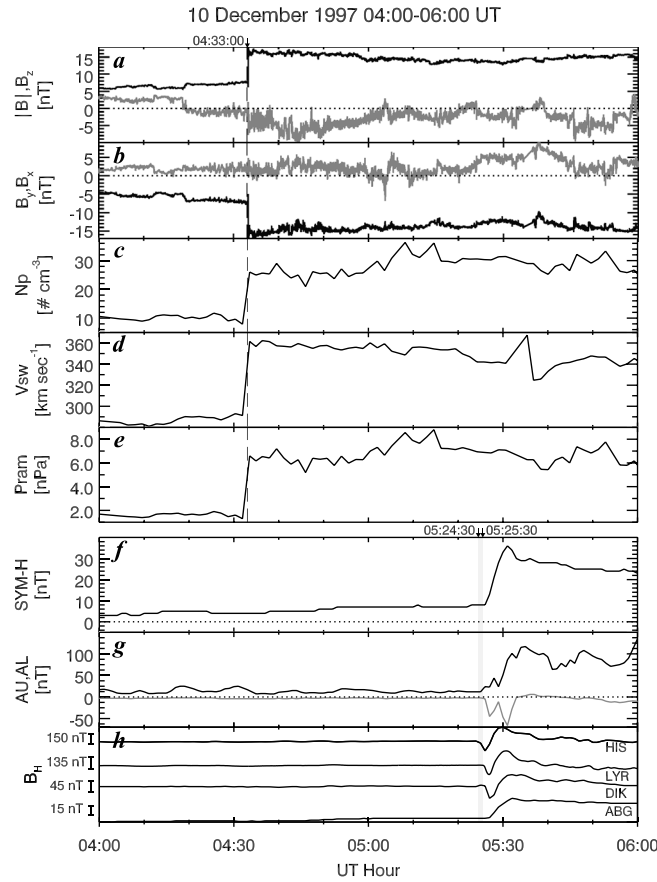


Figure 6. Same as Figure 1, except for 10 December 1997. Horizontal-component magnetograms (h) at Heiss Island (HIS, 75.7° MLAT, 1028 MLT at 0525 UT), Longyearbyen (LYR, 75.2° MLAT, 0830 MLT at 0525 UT), Dixon (DIK, 68.9° MLAT, 1115 MLT at 0525 UT), and Alibag (ABG, 14.1° MLAT, 1031 MLT at 0525 UT).

are shown in Figures 6a–6e. During the shock’s detection by the spacecraft, the magnetic field magnitude increased from 7.5 to 18 nT, and to within 5 nT, held constant through 0600 UT. IMF B_z became increasingly negative but within 5 nT of 0, with a few excursions outside that range. B_y was negative at -7.3 nT and became even more so: reaching -15 nT and remaining less than -12 nT through 0600 UT. There was no significant trend in B_x , which stayed unchanged a few nT above 0 until 0525 UT. From the shock arrival at WIND until 0600 UT, the IMF can generally be described as $B_y \ll B_z < 0, |B_y| \sim |B|$.

Solar wind plasma parameters concurrently jumped. The time of the enhancement is much shorter than the ~ 12 min required for the peak of the solar wind pressure enhancement to occur in the previous case. The combination of an $\sim 18 \text{ cm}^{-3}$ jump in proton density and an $\sim 70 \text{ km s}^{-1}$ increase in solar wind bulk speed resulted in a P_{ram} increase from 1.3 to 6.6 nPa. The rate of pressure increase for this period was 3.3 nPa min^{-1} , more than 10 times that of the previous case. $\Delta P_{\text{ram}}/P_{\text{ram}}$ was about 3.3.

Two different estimates of the shock arrival time, t_0 , at the dayside auroral zone were done by ZT99. Using the location of WIND, solar wind velocity, and shock orientation, they estimated it to be ~ 0525 UT. Using the detection of the shock by Geotail at ~ 0528 UT, located in the dawnside magnetosheath, the authors backpropagated the shock to the subsolar magnetopause, resulting in a time of ~ 0524 UT. Since the response of ground magnetic measurements occurs within 1 min of a sudden change at the magnetopause [Nishida, 1978], the former time is chosen in the current analysis: $t_0 = 0525$ UT with an uncertainty σ_{t_0} of 30 s. It is still useful, however, to verify this with available ground-based magnetic data.

The equatorial SYM-H and high-latitude AU and AL indices are shown in Figures 6f and 6g. Between 0525 and 0526 UT, the AU index doubled to 24 nT, later passing through 100 nT, and remaining elevated through

On the duskside at FSMI (~ 1605 MLT), only diffuse auroral emissions at all wavelengths were observed. There was a 2 min lag of the $\lambda 486.1$ nm channel, after the $\lambda 470.9$ nm occurrence at 0107 UT. Speeds determined from this station are in the range $4.5 \pm 1.4 \text{ km s}^{-1}$.

GILL and RANK are also close in MLT, at about 1810 at t_0 . While there is some spread in time of the shock aurora occurrence between the two stations, both locations register the arrival of shock aurora first in the $\lambda 630.0$ nm, $\lambda 557.7$ nm, and $\lambda 470.9$ nm emissions, followed by $\lambda 486.1$ nm (that is, like the occurrence pattern observed at FSMI). The $\lambda 470.9$ nm emissions from GILL show the shock arrival at 0107 UT, while RANK registers it at 0110 UT. The combined range of speeds for all wavelengths for the two sites is $4.9 \pm 2.2 \text{ km s}^{-1}$.

Discussion of the separation of proton and electron shock auroral occurrence is referred to section 4.

3.2. On 10 December 1997

The WIND spacecraft registered the passage of a fast forward IP shock at 0433 UT on 10 December 1997. At that time, WIND was upstream of Earth at (206, 13, 20) R_E (GSM). Solar wind magnetic field and plasma parameters

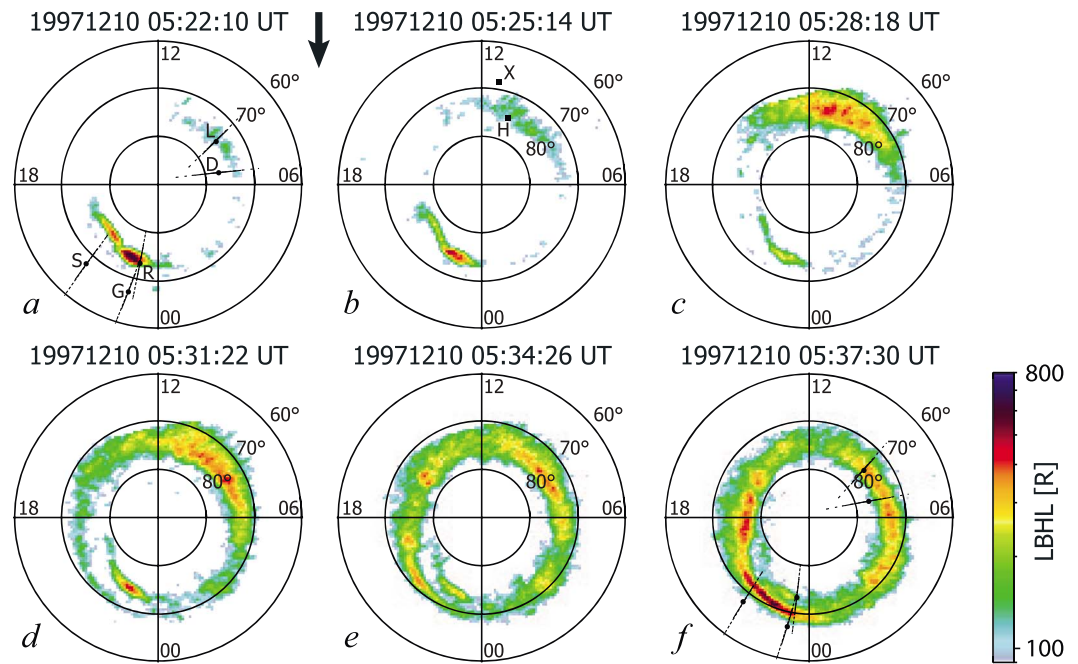


Figure 7. Same as Figure 2, except for 10 December 1997. High-latitude magnetometers closest to m_0 at the shock arrival time t_0 are shown: (H) Heiss Island and (X) Dixon.

0600 UT. The negative turning of B_z and elevated AU suggests enhanced twin-cell convection during this period [e.g., Kamide and Kokubun, 1996]. AL decreased from -2.0 to -4.0 nT between 0525 and 0526 UT. One minute later, it dipped to -45 nT, simultaneously with the first increase of $SYM-H$.

For this case, the estimated location of the initial shock auroral enhancement is $m_0 = 1147$ MLT ± 20 min. High-latitude magnetometers at Dixon and Heiss Island were within 1.5 h MLT of m_0 . Horizontal-component magnetograms from those and the equatorial station Alibag are shown in Figure 6 h. The response from 0525 to 0526 UT at Dixon and Heiss Island was -3 and -29 nT, respectively. The first change at Alibag was 1 nT at 0527 UT and 8 nT at 0528 UT. Given that the earliest unambiguous response, displayed by the AU index and the Dixon and Heiss Island magnetograms occurred between 0524 and 0526 UT, $t_0 = 0525$ UT is confirmed.

Figure 7 illustrates the progression of shock aurora, in a layout identical to Figure 2. Note that the LBHL time series is used again, while ZT99 presented LBHS imagery for this case. The UVI instrument clearly shows the dayside aurora in Figure 7a, centered on the prenoon MLT region owing to the preponderance of negative IMF B_y [Newell et al., 1989; Moen et al., 2001]. The decrease in auroral intensity between the LYR instrument and magnetic noon is also indicative of cusp “midday gap” aurora [Dandekar and Pike, 1978], seen in Figure 7a between 1000 and 1200 MLT. The afternoon side of the midday gap is not observed, possibly owing to it being near the edge of the instrument’s field of view at this time.

Figure 7c shows an unmistakable enhancement of the preexisting aurora, with the average LBHL intensity more than doubling. This is in stark contrast to the relatively subtle enhancement at t_0 for the previous case. By 0531:22 UT (Figure 7d), both the dawnside and duskside intensifications have reached the nightside, later crossing midnight in the 0534:26 UT image (Figure 7e). The image-by-image speed estimate for this case, performed by ZT99, revealed an 11 km s^{-1} propagation speed on the dawnside along 75° MLAT from ~ 0930 to 0430 MLT, between 0526 and 0529 UT. While the same analysis procedure for the duskside was difficult in this instance, the authors report a mean propagation speed of $\sim 8 \text{ km s}^{-1}$ for the interval 0529–0532 UT.

The shock aurora brightening above Longyearbyen, between 0510 and 0610 UT, is shown in Figure 8a in the LBH bands. Comparison of Figures 7c–7f and 8a shows the shock aurora filling a large fraction of the LYR meridian, with an initial, transient equatorward excursion lasting ~ 15 min (0528–0543 UT), followed by a narrowing of the most intense regions as the shock front propagates tailward. When comparing the periods 0510–0525 UT before the shock passage and 0540–0610 UT afterward in Figure 8a, the auroral oval poleward

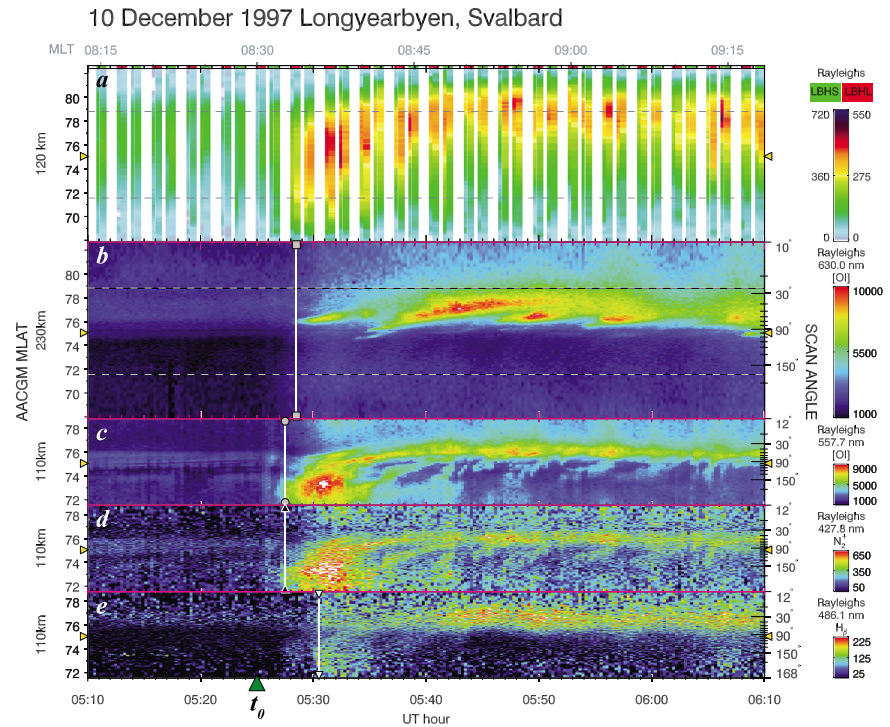


Figure 8. Same as Figure 3, except for 0510–0610 UT on 10 December 1997.

boundary, as shown as the transition between green to light blue in the color scale, moved $\sim 2^\circ$ MLAT poleward. In addition, the overall latitudinal width increased marginally.

In the weaker emissions observed before the arrival of the shock, Figures 8c–8e show a well-defined, roughly constant boundary around 40° – 45° scan angle. The $\lambda 557.7$ nm and $\lambda 427.8$ nm (Figures 8c and 8d) channels show higher emissions equatorward of this boundary, while the $\lambda 486.1$ nm channel (Figure 8e) shows higher emissions poleward of it. The $\lambda 630.0$ nm emissions in Figure 8b also display this step-like feature, but closer to zenith, with two intensity steps at 70° and 100° scan angle. The more northerly boundary (40° – 45° scan angle) is in all likelihood a possible marker for the OCB, to be discussed later. The very sharp intensity minimum between 90° and 98° scan angle, clearly visible in the $\lambda 630.0$ nm and $\lambda 557.7$ nm channels, (Figures 8b and 8c) is an artifact of the MSP optics.

All LYR MSP channels show an increase in emission intensity between 155° and 165° scan angle during the shock arrival. Most pronounced and the earliest to appear are the $\lambda 557.7$ nm (+7 kR) and $\lambda 427.8$ nm (+500 R) emissions, at 0527 UT (Figures 8c and 8d). These are accompanied by minor enhancements in the $\lambda 630.0$ nm (+1.5 kR, Figure 8b) and $\lambda 486.1$ nm (+50 R, Figure 8e) channels. Following the passage of the shock front, $\lambda 557.7$ nm and $\lambda 427.8$ nm emissions near and equatorward of magnetic zenith take the form of elongated and poleward drifting pulsations of ~ 5 – 10 min recurrence period (Figures 8c and 8d).

At 0528 UT, the LYR $\lambda 630.0$ nm channel most prominently displays the shock passage in the form of a narrow, ~ 3.5 kR enhancement between 65° and 75° scan angle, just poleward of the supposed OCB mentioned above (Figure 8b). The poleward motion of this auroral feature, the high-intensity ratio of approximately 2 between $\lambda 630.0$ nm to $\lambda 557.7$ nm, the southward turning of IMF B_z , and the repetition of similar poleward moving auroral forms (PMAFs) beginning at 0534, 0546, and 0553 UT suggest that the source of this precipitation is composed of magnetosheath particles via the IMF B_y -shifted cusp or open LLBL, along newly reconnected flux tubes [Sandholt *et al.*, 1986, 1989; Fasel *et al.*, 1993]. The equatorward edges of the forms are coincident with auroral arc structures, with superposed pulsations on like time scales, in the other three channels. For the channels $\lambda 630.0$ nm, $\lambda 557.7$ nm, and $\lambda 427.8$ nm, the calculated shock propagation speed range is 8.6 ± 2.6 km s^{-1} .

The $\lambda 486.1$ nm channel at LYR reveals the passage of the shock front in two stages (Figure 8e). The first pulse at 0527 UT is morphologically very similar to that in the $\lambda 557.7$ nm and $\lambda 427.8$ nm emissions, with a mean

intensity around ~ 50 R. At 0530 UT a more intense pulse appears, exceeding ~ 100 R. It not only occurs in the same part of the sky as the former but also fills the northern $\sim 50^\circ$ of the meridian, coinciding with the enhanced $\lambda 630.0$ nm emissions and quasi-steady proton aurora already present. Since the main pulse in this channel occurs a few minutes later than the other channels, it is chosen for shock propagation speed analysis, yielding an expectedly smaller value of 4.3 ± 0.4 km s $^{-1}$.

For the diffuse, broad pulse in the southern half of the meridian, $\lambda 486.1$ nm emissions coincident with the latitudinally extended electron aurora pulsations (scan angles $> 80^\circ$ from 0540 to 0610 UT, Figures 8c and 8d) are near the threshold of detectability, yet the equatorward edge of the bulk of the proton auroral emissions dips to lower latitudes (higher scan angles) shortly after the connection of the $\lambda 557.7$ nm and $\lambda 427.8$ nm pulsations to the main auroral band. This is most evident in the $\lambda 486.1$ nm channel at 0543, 0550, and 0558 UT at scan angles 60° – 80° .

Especially for the first pulse of hydrogen emissions at 0527 UT (Figure 8e), it is important to note that electron auroral emissions spectrally near H_β $\lambda 486.1$ nm can be transmitted through the interference filter for this channel of the MSP. The Doppler profile, with rest wavelength $\lambda 486.1$ nm, is typically contaminated on the blue side by the N_2 Vegard Kaplan (VK) (2–15) line at $\lambda 483.7$ nm, and on the red side by [OI] near $\lambda 489.0$ nm. *Stringer* [1971] determined that the VK line could contribute up to 25% of the total signal, with the [OI] lines contributing up to 10%. More generally, the presence of such molecular band emissions forms a semicontinuum near H_β $\lambda 486.1$ nm that acts to vary the background up to the approximate brightness of the line itself [*Lummerzheim et al.*, 2003].

Rules of thumb for determining the amount of electron contamination in hydrogen emission measurements are discussed by *Holmes et al.* [2008] and *Moen et al.* [1998]. Morphological comparisons of H_β $\lambda 486.1$ nm emissions with those commonly created by electrons, such as [OI] $\lambda 557.7$ nm and N_2^+ $\lambda 427.8$ nm, can aid in estimating contamination, as the diffuse nature of proton precipitation does not give rise to discrete auroral forms while electron precipitation can. In the current case, the diffuse character of the aurora observed between 0525 and 0535 UT in the [OI] $\lambda 557.7$ nm and N_2^+ $\lambda 427.8$ nm channels (Figures 8c and 8d), which may have a contribution from proton precipitation via secondary electrons, precludes applying the morphological technique. Instead, the background scans of the $\lambda 486.1$ nm channel are used. Emissions through the slightly shifted passband have been inspected for both the preshock and postshock period, and no appreciable background variation is found in time or scan angle, apart from the increase in emission intensity with increasing zenith angle, a geometric phenomenon known as the van Rhijn effect [*van Rhijn*, 1921]. Thus, there is little contamination from electron emissions passing through the $\lambda 486.1$ nm filter during this period.

The MSP at Danmarkshavn registered the shock-induced auroral enhancement at 0529 UT, with a range of speeds for the two [OI] wavelengths $\lambda 630.0$ nm and $\lambda 557.7$ nm of 8.8 ± 1.0 km s $^{-1}$. The station is at a higher MLAT than LYR, and it detected the poleward portion of the discrete $\lambda 630.0$ nm and more diffuse $\lambda 557.7$ nm emissions, albeit with a longer cadence.

Fort Smith is located in the evening sector at about 2120 MLT at t_0 , and is the first Canadian sector MSP to detect the shock passage. In Figure 9, note that while light pollution affects the southern half of the meridian scans, especially between 0510 and 0525 UT, the shock aurora appears in the northern half. When comparing the evolution of the shock aurora along the dawnside and duskside of the auroral oval in Figure 7, it is apparent that the auroral intensification is more discontinuous on the duskside. The LBH band keogram in Figure 9a corroborates this, with an intensification above 1 kR (600 R) for the LBHS (LBHL) band at ~ 0534 UT.

A similar evolution of shock aurora features is shown in Figures 9b–9e. The intensifications in the LBH bands are easily identifiable in the MSP channels, with $\lambda 557.7$ nm and $\lambda 470.9$ nm being most pronounced (Figures 9c and 9d). The $\lambda 557.7$ nm channel also clearly shows the overall equatorward auroral expansion after the shock impingement through 0610 UT (Figure 9c). Comparison of Figures 9a–9c suggests a partially bifurcated evolution, with two discernible arc-like structures, upon which the above mentioned intensifications are superposed. However, given the coarse spatial resolution of the data, that the two structures are local maxima of an otherwise diffuse auroral band cannot be ruled out. In addition, the quasiperiodicity of between 10 and 20 min of the enhancements in Figures 9a–9d suggests pseudobreakup activity. At Fort Smith, the shock onset time for the channels $\lambda 630.0$ nm, $\lambda 557.7$ nm, and $\lambda 470.9$ nm was found to be 0533 UT, with a determined shock propagation speed of 5.3 ± 0.6 km s $^{-1}$.

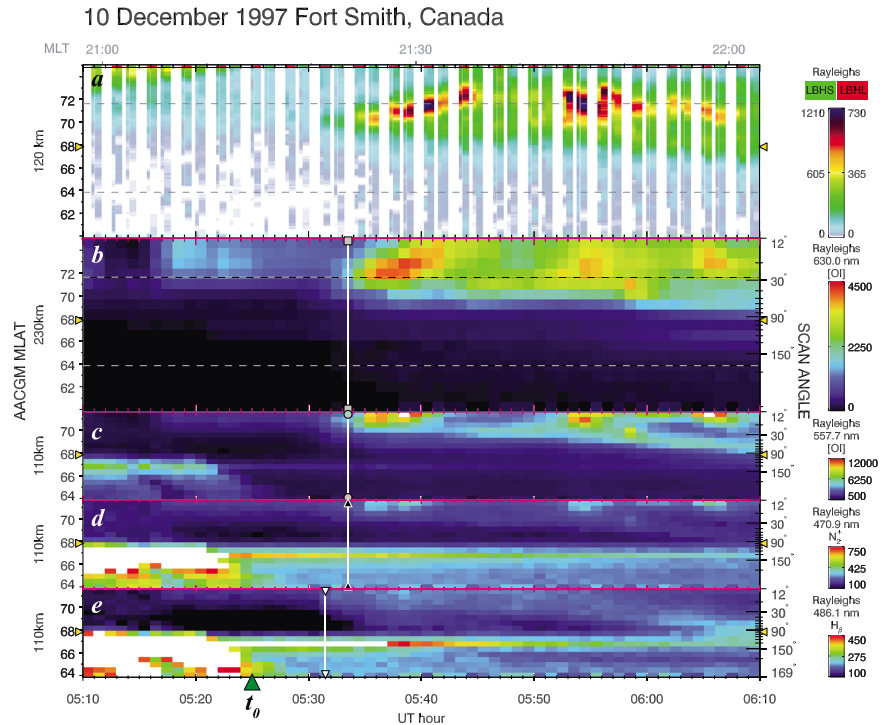


Figure 9. Same as Figure 4, except for Fort Smith (FSMI) between 0510 and 0610 UT on 10 December 1997. Scattered terrestrial light reflected from cloud cover is seen in the southern half of the meridian in Figures 9c–9e, especially between 0510 and 0524 UT.

The FSMI $\lambda 486.1$ nm channel shows similar equatorward drift, but it is unsurprisingly more spatially diffuse (Figure 9e). Of the two above mentioned maxima, the more equatorial one is associated with higher hydrogen emissions: more than 250 R between 0600 and 0610 UT. Interestingly, the time of shock impingement with this channel is 2 min earlier than the others, occurring at 0531 UT at the lowest scan angles on the northern horizon. The shock speed for this channel is 8.2 ± 1.0 km s⁻¹.

The MLT and UT time coordinates of shock-induced auroral enhancement for this case are shown in Figure 10. The average energy flux values show less preshock dayside aurora and lower peak energy flux values during the propagation of the shock than in the previous case. In addition, the previously mentioned discontinuous deposition of electron auroral energy on the duskside is apparent also.

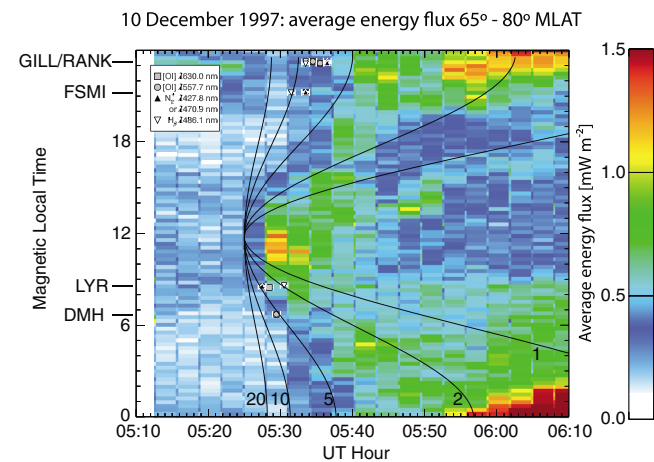


Figure 10. Same as Figure 5, except for 10 December 1997, between 0510 and 0610 UT. In this case, m_0 was 1147 MLT. Constant speed contours [km s⁻¹] correspond to 73.9° ($0 < \text{MLT} < 12$) and 70.8° MLAT ($12 < \text{MLT} < 24$).

Collectively, the duskside MSPs all detect the arrival of shock-induced hydrogen emissions ($\lambda 486.1$ nm) before the other channels. At FSMI, the enhancement occurred at 0531 UT, while the other channels detected it at 0533 UT. Similar ranges were encountered for GILL and RANK. All three instruments recorded diffuse aurora with enhancements occurring with a 10–20 min periodicity, as shown in the FSMI keogram (Figures 9b–9d).

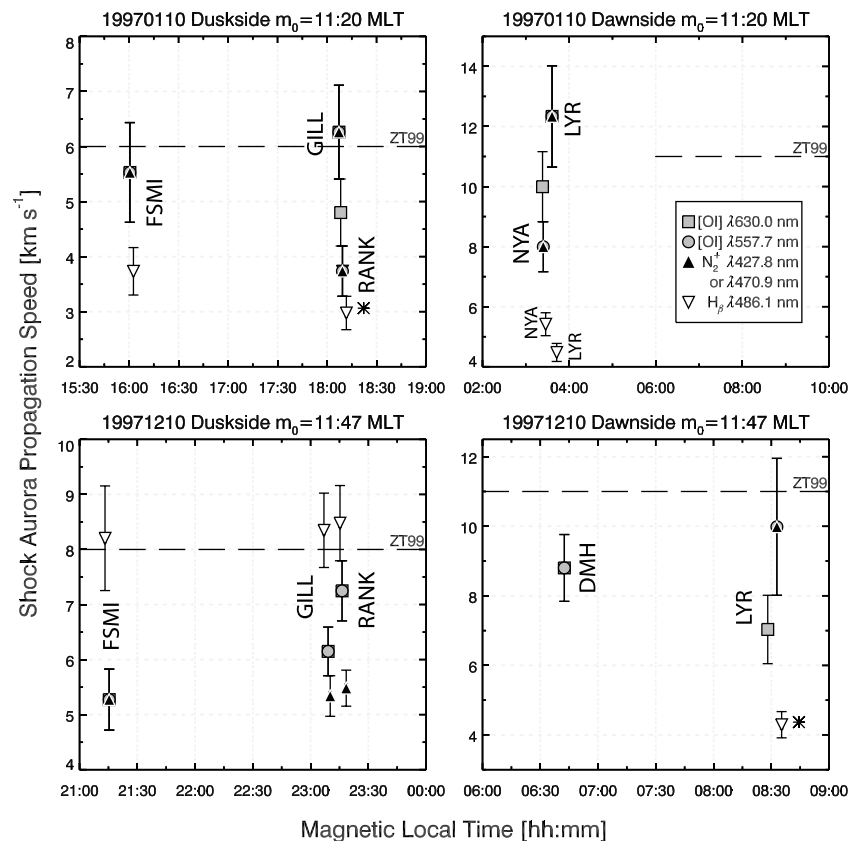


Figure 11. Shock auroral propagation speeds starting from m_0 at time t_0 to the moment of detection above each MSP (t_{ij}) for both the January and December 1997 cases. Canadian sector (duskside) speeds in the left column; Greenlandic and Scandinavian (dawnside) speeds in the right column. The dashed, horizontal lines represent the speeds reported, with limits in MLT if specified, by ZT99. Symbols correspond to MSP channels, consistent with previous figures. Asterisks denote two-pulse shock arrivals observed in the H_β ($\lambda 486.1$ nm) channel, the plotted speed corresponding to the second pulse.

4. Discussion and Conclusions

The two cases considered are examples of the effects of solar wind shocks on two totally different solar wind, magnetospheric, and auroral configurations. Estimation of m_0 from the shock orientation, t_0 from magnetometer and geomagnetic indices, and the t_{ij} from MSPs with 1 min time resolution yields shock aurora propagation speeds along the auroral oval that agree generally with those reported by ZT99. This further confirms the previously held notion that the speed of the shock in the solar wind approximately matches the speed along the auroral oval. Figure 11 illustrates the determined speeds for both analyzed cases.

On the duskside for 10 January 1997, the determined shock propagation speed by ZT99, 6 km s^{-1} , is shown as a dashed line in Figure 11 (top left). The auroral enhancements in $\lambda 630.0$ nm (gray squares), $\lambda 557.7$ nm (gray circles), and $\lambda 470.9$ nm (black triangles), detected earliest by the MSPs at FSMI and GILL, agree with this value to within calculated uncertainties. Since RANK records the shock arrival in the above mentioned channels later, the speeds are correspondingly slower.

Hydrogen shock aurora emissions (white triangles) detected on the duskside occur after those of $\lambda 470.9$ nm (black triangles) and both metastable atomic oxygen lines (gray squares and circles). However, it is noteworthy that RANK did detect a two-pulse H_β $\lambda 486.1$ nm sequence (denoted by asterisk symbol in Figure 11), first reported optically in shock aurora by *Motoba et al.* [2009]. Their study attributed the first pulse (measured at ~ 1500 MLT) mainly to proton precipitation. In the framework of the SC model of *Araki* [1994], the FAC associated with this Preliminary Impulse (PI) is downward in the afternoon sector and would be composed of mainly precipitating protons (cf. downward current C1 in Figure 14 in *Araki* [1994]). The main impulse (MI) that follows was made of mostly electrons flowing in an upward current (cf. current C2 in Figure 14 in *Araki* [1994]).

Despite the later MLT (~1815), the double-pulse sequence observed at RANK is morphologically similar. A short PI is observed in $\lambda 486.1$ nm (Figure 4e), peaking at 0109 UT, followed by the MI at 0111 UT. The later pulse is also accompanied by a latitudinally narrow, discrete electron arc in Figures 4c and 4d, a minute after shock arrival (two bright pixels at 0111 UT, 50–60° scan angle). Magnetometer data from RANK (1 min resolution, Figure 1 h) show a minor negative excursion in the H component, followed by a stronger, positive one at the above times [Mann *et al.*, 2008]. This is potentially in agreement with FACs predicted by the Araki [1994] model, although it does not allow for the presence of both C1 and C2 at such a late MLT. The recommendation to extend the model to later MLTs has previously been discussed [Lam and Rodger, 2001]. Why FSMI and GILL do not detect the two-pulse H_β signature is a matter of speculation and could be owing to the shock aurora passage being observed beyond the northern limit of the instruments' meridians.

For the same case on the dawnside, $\lambda 630.0$ nm, $\lambda 557.7$ nm, and $\lambda 4278$ nm channels (Figures 3b–3d) at LYR detect the shock aurora with an estimated speed of 12.3 ± 1.7 km s⁻¹, in approximate agreement with 11 km s⁻¹ reported by ZT99. NYA observed the shock arrival in the same emissions, spread between 0108 and 0110 UT, resulting in a slower shock propagation speed. The difference between the two sites has partially to do with observing geometry, with the scan planes of the instruments not being exactly collinear. As seen from Figure 2a, the LYR scan plane is oriented slightly anticlockwise relative to the plane of NYA. Thus, the southern portion of the LYR scan plane reaches later MLTs than NYA, registering the shock aurora sooner. Both locations recorded a single-pulse $\lambda 486.1$ nm shock occurrence some minutes later, with propagation speed between ~4 and 6 km s⁻¹.

Interpretation of the relative amounts of diffuse and discrete aurora for this case suggests all locations detect diffuse, quasi-steady, $\lambda 557.7$ nm dominated shock aurora in the equatorward portion of the auroral oval, ostensibly originating from the CPS near noon and possibly the dayside extension of the BPS along the flanks, on closed field lines. The RANK MSP on the duskside has the best viewing geometry and shows somewhat structured arcs overhead and to the north that are semicontinuous in time and slowly progress equatorward. Another hypothesis is that boreal (IMF $B_x < 0$) lobe reconnection occurred tailward of the cusp, and the source of the enhanced auroral particles came instead from capture of dense magnetosheath plasma from the LLBL [Sandholt *et al.*, 1999]. Unfortunately, there were no MSPs close to local noon to add the needed detail for confirmation.

The best observations of discrete arcs found poleward of the diffuse aurora are at LYR and NYA. Such well-defined arcs near zenith between 0110 and 0125 UT are type 4 aurora, originating from precipitating BPS electrons (after categorization established by Sandholt *et al.* [1998]). They are found poleward of the diffuse auroral band, manifest as multiple arc systems elongated in longitude, and thought to be auroral signatures of momentum and plasma transfer between the solar wind, magnetosheath, and magnetosphere via the flank boundary layers [Sandholt *et al.*, 2002]. A previous study performed a tracing of field lines threading discrete type 4 arcs near 0900 MLT, albeit influenced by a more steady state solar wind, and found either open field lines or closed field lines that map to the distant magnetotail [Ober *et al.*, 2000]. Given that shock-induced auroral arcs reported here appear above the Svalbard MSPs closer to 0330 MLT, the latter mapping is much more likely.

The 10 December 1997 case reveals a different development of shock auroral occurrence on the duskside. For all three Canadian sector MSPs, located within a few hours of magnetic midnight, the H_β $\lambda 486.1$ nm channel registered the shock arrival first. The mean shock propagation speed reported by ZT99 for the duskside is 8 km s⁻¹, while the respective H_β $\lambda 486.1$ nm speeds from FSMI, GILL, and RANK were 8.2 ± 1.0 , 8.3 ± 0.7 , and 8.5 ± 0.7 km s⁻¹ (cf. Figure 11, bottom left). The MSP-determined shock speeds are all slightly higher than the ZT99 value but agree to within uncertainties. Also different in this case is the lack of a definitive dual-pulse H_β $\lambda 486.1$ nm signature. However, it might not be expected at such MLTs close to midnight.

At the moment of shock arrival, FSMI and GILL are again too equatorward to observe any possible discrete electron auroral structures poleward of the diffuse shock-induced brightening they did detect. It is possible that the MSP at RANK did observe both types of initial shock aurora, but the spatial resolution is too low to be certain. The presence of an isolated auroral spot in the RANK FOV (Figure 7a between 2200 and 2300 MLT) renders the discrimination between preexisting and shock aurora difficult. However, Figures 7e–7f show the propagation of shock aurora to cross the RANK meridian equatorward of the spot, resulting in a double auroral oval from approximately 1900 MLT through midnight. The enhanced, shock-induced aurora being spatially separate from the preexisting spot makes timing of the shock arrival possible.

On 10 December 1997 at ~0525 UT, the DMH and LYR instruments are located postdawn at 0630 and 0830 MLT, respectively. At LYR, diffuse aurora observed in $\lambda 557.7$ nm and $\lambda 427.8$ nm (Figures 8c and 8d) and also weakly in $\lambda 486.1$ nm (Figure 8e) abruptly fills the southern meridian at onset. The propagation speed for this event in the $\lambda 557.7$ nm and $\lambda 427.8$ nm channels was 10 ± 2.0 km s⁻¹, in agreement with the previously published value of 11 km s⁻¹ (Figure 11, bottom right). A narrow $\lambda 630.0$ nm-dominated PMAF appears poleward of that a minute later (Figure 8b), followed by a second, more intense H_{β} $\lambda 486.1$ nm pulse (Figure 8e). This two-pulse H_{β} $\lambda 486.1$ nm sequence was unfortunately not detected at DMH, as H_{β} data were not acquired.

The morphology of the two-pulse sequence in the Longyearbyen $\lambda 486.1$ nm channel also fits in the SC model of Araki [1994]. Figure 6h shows the H component magnetogram (10 s resolution) for LYR. At 05:26:30 UT, the negative excursion of the trace peaks and is associated with an upward FAC in response to the PI. Following at 05:30:45 UT, the component goes through a positive maximum, coincident with the MI and the onset of significant proton precipitation (Figure 8e) and a downward FAC. In the model of Araki [1994], the prenoon MI location is fixed at 0840 MLT and 75° MLAT, which is very close to what is observed at LYR for the considered case. However, others have noted that the arbitrariness of the locations of these FAC systems is an attempt to depict a nominal global response to shock onsets [Lam and Rodger, 2001; Vontrat-Reberac et al., 2002].

The PMAFs observed mostly in $\lambda 630.0$ nm (Figure 8b) are indicative of soft electron precipitation and often have a complement of hydrogen $\lambda 486.1$ nm emissions, as is the case here [Sandholt et al., 1993; Fasel et al., 1993]. They are routinely observed in and near the cusp and are related to flux transfer events and/or variations in the magnetopause reconnection rate during periods of negative IMF B_z [Moen et al., 2001]. Owing to the sudden increased negative IMF B_z during the shock impingement, subsolar magnetopause reconnection is possible; one auroral manifestation of which is PMAFs located at the footpoints of newly reconnected flux tubes [Sandholt et al., 1986; Fasel et al., 1993]. Given the prevailing IMF conditions after the shock impingement ($B_z < 0$; $B_y < 0$), the PMAFs observed fall into the category of PMAFs/prenoon/ $B_y < 0$, after the categorization of Sandholt and Farrugia [2007]. In addition, the presence of pulsed proton events as periodic enhancements in the H_{β} $\lambda 486.1$ nm signatures coincident with the PMAFs implies precipitation of both protons and electrons along newly opened magnetic flux [Sigernes et al., 1996; Deehr et al., 1998; Lorentzen and Moen, 2000].

The shock-induced transition of IMF B_y from slightly negative to increasingly so supports the notion that the forms observed are located on open field lines, as negative IMF B_y acts to shift the cusp/LLBL region dawnward toward the LYR MSP at ~0830 MLT [Newell et al., 1989; Moen et al., 2001]. Furthermore, the zonal width of the cusp is known to increase when subject to sudden pressure enhancements [Newell and Meng, 1994]. Thus, the occurrence of soft, discrete precipitation under the influence shock-induced magnetopause reconnection is expected to originate on open field lines in either the open LLBL or cusp regions. During and after the shock passage, the interface between the pulsating, diffuse aurora and PMAFs is a marker for the OCB, supporting the finding that shocked dayside auroral forms are governed by field line status even as early as 0830 MLT [Zhou et al., 2009].

In summary, two cases of shock-induced aurora are reexamined using a distributed array of meridian scanning photometers in the Northern Hemisphere. Estimating the location and time of the initial shock aurora brightening combined with 1 min or higher time resolution MSP data results in speeds of shock aurora progression that are compared with the initial calculated speeds, using coarser timing, of Zhou and Tsurutani [1999]. While the cases were previously studied using satellite imaging, the addition of distributed optical instruments contributes to the quite small number of cases where the response of the dayside aurora to shocks is observed, in fine detail, from the ground [e.g., Sandholt et al., 1994, 1998; Lorentzen and Moen, 2000; Kozlovsky et al., 2005; Motoba et al., 2009; Zhou et al., 2009; Liu et al., 2011].

In general, the average speed of shock arrival, determined from the first observable shock aurora in a given MSP channel agrees with previously reported values to within reasonable uncertainties. The data also reveal the following details unobservable from satellite imaging alone: (1) the shock auroral progression on 10 January 1997 reveals hydrogen emissions at $\lambda 486.1$ nm from precipitating protons occurring after discrete features (1–2 min on the duskside, 3–6 min on the dawnside) presumed to result from precipitating electrons. The exception to this is the PI-associated (i.e., initial) proton auroral pulse observed at RANK for this case. However, this PI proton auroral pulse was not detected at the two other duskside locations. (2) The duskside progression on 10 December 1997 showed diffuse shock auroras in H_{β} $\lambda 486.1$ nm appearing from 1 to 3 min

earlier than diffuse and discrete aurora in other channels. (3) MSPs at the highest magnetic latitudes with an H_p 2486.1 nm channel, RANK and LYR, were well positioned to detect a two-pulse proton auroral response to the shock. The two-pulse proton auroral event at LYR on 10 December 1997 (0830 MLT) was found to qualitatively agree with the model predictions of Araki [1994] for prenoon shock-induced FACs. Observations of two-pulse proton auroral onset at RANK appear to also agree with the model predictions, but at a later MLT than the coverage of the model. Two-pulse proton auroral onsets were not observed by other MSPs for the two cases. (4) Shocked dayside aurora in/near the cusp on 10 December 1997 above Svalbard occurred as soft, 2630.0 nm dominated PMAFs and pulsed proton events on newly reconnected field lines. Equatorward of that, pulsating, diffuse, and possibly harder proton and electron aurora was observed, in a manner similar to the case reported by Zhou *et al.* [2009], but at a somewhat earlier MLT.

Acknowledgments

This effort was supported in part by the Air Force Office of Scientific Research. It was also supported by the Research Council of Norway/CoE under contract 223252/F50 and by the Research Council of Norway under contract 195385/V30. C.S.D. acknowledges support from the National Science Foundation Award ATM-0334800. We thank the principal investigator on the SWE investigation, K. Ogilvie, and the MFI investigation on WIND, R. P. Leppig, for use of the data. Thanks also to POLAR principal investigator G. Parks for use of the UVI data. Operational support for the NORSTAR (formerly CANOPUS) instrument array was provided by the Canadian Space Agency. We acknowledge the efforts of Fokke Creutzberg who was principally responsible for the scientific operation of the CANOPUS meridian scanning photometer array. We are also grateful to Greg Baker and Emma Spanswick for providing data and helpful instrument details. We thank Tromsø Geophysical Observatory of UiT, The Arctic University of Norway, for providing the magnetometer data from Longyearbyen. The authors also thank I. R. Mann, D. K. Milling and the rest of the CARISMA team for Rankin Inlet magnetometer data. CARISMA is operated by the University of Alberta, funded by the Canadian Space Agency. Other magnetometer data were obtained via the SPIDR database, maintained by the National Geophysical Data Center (NGDC) of the National Atmospheric and Oceanographic Administration (NOAA). We acknowledge instrument custodians for individual magnetometer stations and for the MSPs at Danmarkshavn and Ny-Ålesund. All data used in this work are freely available from the relevant networks and/or institutions. Thanks also to Espen Trondsen for providing University of Oslo MSP data. J.M.H. thanks Dirk Lummerzheim and colleagues at Air Force Research Laboratory for helpful software and discussions.

Robert Lysak thanks Athanasios Boudouridis and another reviewer for their assistance in evaluating this paper.

References

- Araki, T. (1994), A physical model of geomagnetic sudden commencement, in *Solar Wind Sources of Magnetospheric Ultra-Low-Frequency Waves*, *Geophys. Monogr. Ser.*, vol. 81, edited by M. J. Engebretson, K. Takahashi, and M. Scholer, p. 183, AGU, Washington, D. C.
- Arballo, J. K., *et al.* (1998), Pseudobreakups during January 10, 1997, in *International Conference on Substorms-4*, edited by Y. Kamide and S. Kokubun, pp. 315–318, Terra Sci., Tokyo.
- Baker, K. B., and S. Wing (1989), A new magnetic coordinate system for conjugate studies at high latitudes, *J. Geophys. Res.*, *94*(A7), 9139–9143, doi:10.1029/JA094iA07p09139.
- Berdichevsky, D. B., A. Szabo, R. P. Leppig, A. F. Viñas, and F. Mariani (2000), Interplanetary fast shocks and associated drivers observed through the 23rd solar minimum by Wind over its first 2.5 years, *J. Geophys. Res.*, *105*(A12), 27,289–27,314, doi:10.1029/1999JA000367.
- Blagoveshchensky, D. V., and V. A. Kornienko (2007), Studying the ionosphere with the incoherent scatter radar during the magnetic storm of January 10, 1997, *Geomagnetizm i Aeronomiya*, *47*, 242–253, doi:10.1134/S0016793207020119.
- Boudouridis, A., E. Zesta, L. R. Lyons, P. C. Anderson, and D. Lummerzheim (2003), Effect of solar wind pressure pulses on the size and strength of the auroral oval, *J. Geophys. Res.*, *108*(A4), 8012, doi:10.1029/2002JA009373.
- Boudouridis, A., E. Zesta, L. R. Lyons, P. C. Anderson, and D. Lummerzheim (2005), Enhanced solar wind geoeffectiveness after a sudden increase in dynamic pressure during southward IMF orientation, *J. Geophys. Res.*, *110*, A05214, doi:10.1029/2004JA010704.
- Boudouridis, A., L. R. Lyons, E. Zesta, and J. M. Ruohoniemi (2007), Dayside reconnection enhancement resulting from a solar wind dynamic pressure increase, *J. Geophys. Res.*, *112*, A06201, doi:10.1029/2006JA012141.
- Boudouridis, A., L. R. Lyons, E. Zesta, J. M. Weygand, A. J. Ribeiro, and J. M. Ruohoniemi (2011), Statistical study of the effect of solar wind dynamic pressure fronts on the dayside and nightside ionospheric convection, *J. Geophys. Res.*, *116*, A10233, doi:10.1029/2011JA016582.
- Brittnacher, M., M. Wilber, M. Fillingim, D. Chua, G. Parks, J. Spann, and G. Germany (2000), Global auroral response to a solar wind pressure pulse, *Adv. Space Res.*, *25*, 1377–1385.
- Cerisier, J.-C., A. Marchaudon, J.-M. Bosqued, K. McWilliams, H. U. Frey, M. Bouhram, H. Laakso, M. Dunlop, M. Förster, and A. Fazakerley (2005), Ionospheric signatures of plasma injections in the cusp triggered by solar wind pressure pulses, *J. Geophys. Res.*, *110*, A08204, doi:10.1029/2004JA010962.
- Chua, D., G. Parks, M. Brittnacher, W. Peria, G. Germany, J. Spann, and C. Carlson (2001), Energy characteristics of auroral electron precipitation: A comparison of substorms and pressure pulse related auroral activity, *J. Geophys. Res.*, *106*, 5945–5956, doi:10.1029/2000JA003027.
- Coco, I., E. Amata, M. F. Marcucci, D. Ambrosino, J.-P. Villain, and C. Hanuise (2008), The effects of an interplanetary shock on the high-latitude ionospheric convection during an IMF B_y -dominated period, *Ann. Geophys.*, *26*, 2937–2951, doi:10.5194/angeo-26-2937-2008.
- Craven, J. D., L. A. Frank, C. T. Russell, E. E. Smith, and R. P. Leppig (1986), Global auroral responses to magnetospheric compressions by shocks in the solar wind: Two case studies, in *Solar Wind-Magnetosphere Coupling*, edited by Y. Kamide and J. A. Slavin, 367 pp., Terra Sci., Tokyo, Japan.
- Deehr, C. S., D. A. Lorentzen, F. Sigernes, and R. W. Smith (1998), Dayside auroral hydrogen emission as an aeronomical signature of magnetospheric boundary layer processes, *Geophys. Res. Lett.*, *25*(12), 2111–2114, doi:10.1029/98GL01535.
- Dendekar, B. S., and C. P. Pike (1978), The midday discrete auroral gap, *J. Geophys. Res.*, *83*, 4227–4236, doi:10.1029/JA083iA09p04227.
- Echer, E., B. T. Tsurutani, F. L. Guarnieri, and J. U. Kozmyra (2011), Interplanetary fast forward shocks and their geomagnetic effects: CAWSES events, *J. Atmos. Sol. Terr. Phys.*, *73*, 1330–1338, doi:10.1016/j.jastp.2010.09.020.
- Farrugia, C. J., P. E. Sandholt, J. Moen, and R. L. Arnoldy (1998), Unusual features of the January 1997 magnetic cloud and their effect on optical dayside auroral signatures, *Geophys. Res. Lett.*, *25*(15), 3051–3054, doi:10.1029/98GL01226.
- Fasel, G. J., L. C. Lee, and R. W. Smith (1993), A mechanism for the multiple brightenings of dayside poleward-moving auroral forms, *Geophys. Res. Lett.*, *20*(20), 2247–2250, doi:10.1029/93GL02487.
- Fox, N. J., M. Peredo, and B. J. Thompson (1998), Cradle to grave tracking of the January 6–11, 1997 Sun-Earth connection event, *Geophys. Res. Lett.*, *25*(14), 2461–2464, doi:10.1029/98GL01775.
- Fuselier, S. A., S. P. Gary, M. F. Thomsen, E. S. Claflin, H. Hubert, B. R. Sandel, and T. Immel (2004), Generation of transient dayside subauroral proton precipitation, *J. Geophys. Res.*, *109*, A12227, doi:10.1029/2004JA010393.
- Galand, M., and D. Lummerzheim (2004), Contribution of proton precipitation to space-based auroral FUV observations, *J. Geophys. Res.*, *109*, A03307, doi:10.1029/2003JA010321.
- Germany, G. A., M. R. Torr, D. G. Torr, and P. G. Richards (1994), Use of FUV auroral emissions as diagnostic indicators, *J. Geophys. Res.*, *99*, 383–388, doi:10.1029/93JA02357.
- Han, D.-S., T. Araki, H.-G. Yang, Z.-T. Chen, T. Iyemori, and P. Stauning (2007), Comparative study of geomagnetic sudden commencement (SC) between Oersted and ground observations at different local times, *J. Geophys. Res.*, *112*, A05226, doi:10.1029/2006JA011953.
- Holmes, J. M., B. V. Kozelov, F. Sigernes, D. A. Lorentzen, and C. S. Deehr (2008), Dual site observations of dayside Doppler-shifted hydrogen profiles: Preliminary results, *Can. J. Phys.*, *86*(5), 691–698, doi:10.1139/p08-026.
- Johnsen, M. G., D. A. Lorentzen, J. M. Holmes, and U. P. Løvhaug (2012), A model based method for obtaining the open/closed field line boundary from the cusp auroral 6300 Å [OI] red line, *J. Geophys. Res.*, *117*, A03319, doi:10.1029/2011JA016980.
- Kamide, Y., and S. Kokubun (1996), Two-component auroral electrojet: Importance for substorm studies, *J. Geophys. Res.*, *101*(A6), 13,027–13,046, doi:10.1029/96JA00142.

- Knight, H. K., D. J. Strickland, J. H. Hecht, P. R. Straus, D. Morrison, L. J. Paxton, and D. S. Evans (2008), Evidence for significantly greater N_2 Lyman-Birge-Hopfield emission efficiencies in proton versus electron aurora based on analysis of coincident DMSP SSUSI and SSJ/5 data, *J. Geophys. Res.*, *113*, A04305, doi:10.1029/2007JA012728.
- Kozlovsky, A., V. Safargaleev, N. Østgaard, T. Turunen, A. Koustov, J. Jussila, and A. Roldugin (2005), On the motion of dayside auroras caused by a solar wind pressure pulse, *Ann. Geophys.*, *23*, 509.
- Kozlovsky, A., M. Meurant, and T. Turunen (2007), Changes of dayside auroral distribution caused by a solar wind pressure pulse and associated interplanetary magnetic field disturbances, *Ann. Geophys.*, *25*, 929–940, doi:10.5194/angeo-25-929-2007.
- Lam, M. M., and A. S. Rodger (2001), A case study test of Araki's physical model of geomagnetic sudden commencement, *J. Geophys. Res.*, *106*(A7), 13,135–13,144, doi:10.1029/2000JA900134.
- Laundal, K. M., and N. Østgaard (2008), Persistent global proton aurora caused by high solar wind dynamic pressure, *J. Geophys. Res.*, *113*, A08231, doi:10.1029/2008JA013147.
- Liou, K., C.-C. Wu, R. P. Lepping, P. T. Newell, and C.-I. Meng (2002), Midday sub-auroral patches (MSPs) associated with interplanetary shocks, *Geophys. Res. Lett.*, *29*(16), 1771, doi:10.1029/2001GL014182.
- Liou, K., P. T. Newell, J.-H. Shue, C.-I. Meng, Y. Miyashita, H. Kojima, and H. Matsumoto (2007), "Compression aurora": Particle precipitation driven by long-duration high solar wind ram pressure, *J. Geophys. Res.*, *112*, A11216, doi:10.1029/2007JA012443.
- Liu, J. J., H. Q. Hu, D. S. Han, T. Araki, Z. J. Hu, Q. H. Zhang, H. G. Yang, N. Sato, A. S. Yukimatu, and Y. Ebihara (2011), Decrease of auroral intensity associated with reversal of plasma convection in response to an interplanetary shock as observed over Zhongshan station in Antarctica, *J. Geophys. Res.*, *116*, A03210, doi:10.1029/2010JA016156.
- Lockwood, M., P. E. Sandholt, S. W. H. Cowley, and T. Oguti (1989), Interplanetary magnetic field control of dayside auroral activity and the transfer of momentum across the dayside magnetopause, *Planet. Space Sci.*, *37*, 1347–1365.
- Lorentzen, D. A. (2000), Latitudinal and longitudinal dispersion of energetic auroral protons, *Ann. Geophys.*, *18*, 81–89, doi:10.1007/s00585-000-0081-3.
- Lorentzen, D. A., and J. Moen (2000), Auroral proton and electron signatures in the dayside aurora, *J. Geophys. Res.*, *105*(A6), 12,733–12,745, doi:10.1029/1999JA900405.
- Lorentzen, D. A., P. M. Kintner, J. Moen, F. Sigernes, K. Oksavik, Y. Ogawa, and J. Holmes (2007), Pulsating dayside aurora in relation to ion upflow events during a northward interplanetary magnetic field (IMF) dominated by a strongly negative IMF B_y , *J. Geophys. Res.*, *112*, A03301, doi:10.1029/2006JA011757.
- Lummerzheim, D., M. Galand, and M. Kubota (2003), Optical emissions from proton aurora, in *Proc. of 28th Annual Optical Meeting, Sodankylä Geophysical Observatory Publications*, vol. 92, edited by K. U. Kaila, J. R. T. Jussila, and H. Holma, pp. 1–5, Sodankylä Geophysical Observatory Publications, Finland.
- Lyons, L. R., E. Zesta, J. C. Samson, and G. D. Reeves (2000), Auroral disturbances during the January 10, 1997 magnetic storm, *Geophys. Res. Lett.*, *27*(20), 3237–3240, doi:10.1029/1999GL000014.
- Mann, I. R., et al. (2008), The upgraded CARISMA magnetometer array in the THEMIS era, *Space Sci. Rev.*, *141*, 413–501, doi:10.1007/s11214-008-9457-6.
- McEwen, D. J., D. P. Steele, F. Creutzberg, and D. D. Wallis (1999), The ionospheric response to the CME event of 6–11 January 1997, *J. Atmos. Sol. Terr. Phys.*, *61*, 223–232, doi:10.1016/S1364-6826(98)00140-0.
- Meurant, M., J.-C. Gérard, B. Hubert, V. Coumans, C. Blockx, N. Østgaard, and S. B. Mende (2003), Dynamics of global scale electron and proton precipitation induced by a solar wind pressure pulse, *Geophys. Res. Lett.*, *30*(20), 2032, doi:10.1029/2003GL018017.
- Meurant, M., J.-C. Gérard, C. Blockx, B. Hubert, and V. Coumans (2004), Propagation of electron and proton shock-induced aurora and the role of the interplanetary magnetic field and solar wind, *J. Geophys. Res.*, *109*, A10210, doi:10.1029/2004JA010453.
- Meurant, M., J.-C. Gérard, C. Blockx, V. Coumans, B. Hubert, M. Connors, L. R. Lyons, and E. Donovan (2005), Comparison of intense nightside shock-induced precipitation and substorm activity, *J. Geophys. Res.*, *110*, A07228, doi:10.1029/2004JA010916.
- Moen, J., D. A. Lorentzen, and F. Sigernes (1998), Dayside moving auroral forms and bursty proton auroral events in relation to particle boundaries observed by NOAA 12, *J. Geophys. Res.*, *103*(A7), 14,855–14,863, doi:10.1029/97JA02877.
- Moen, J., P. E. Sandholt, and A. Egeland (2001), Pre- and post-noon asymmetry in dayside auroral activity and convection related to solar wind-magnetosphere interactions, *Adv. Space Res.*, *27*, 1363–1372, doi:10.1016/S0273-1177(01)00031-X.
- Motoba, T., A. Kadokura, Y. Ebihara, H. U. Frey, A. T. Weatherwax, and N. Sato (2009), Simultaneous ground-satellite optical observations of postnoon shock aurora in the Southern Hemisphere, *J. Geophys. Res.*, *114*, A07209, doi:10.1029/2008JA014007.
- Newell, P. T., and C.-I. Meng (1994), Ionospheric projections of magnetospheric regions under low and high solar wind pressure conditions, *J. Geophys. Res.*, *99*(A1), 273–286, doi:10.1029/93JA02273.
- Newell, P. T., C.-I. Meng, D. G. Sibeck, and R. Lepping (1989), Some low-altitude cusp dependencies on the interplanetary magnetic field, *J. Geophys. Res.*, *94*(A7), 8921–8927, doi:10.1029/JA094iA07p08921.
- Nishida, A. (1978), *Geomagnetic Diagnosis of the Magnetosphere*, Springer-Verlag, New York.
- Ober, D. M., N. C. Maynard, W. J. Burke, J. Moen, A. Egeland, P. E. Sandholt, C. J. Farrugia, E. J. Weber, and J. D. Scudder (2000), Mapping prenoon auroral structures to the magnetosphere, *J. Geophys. Res.*, *105*(A12), 27,519–27,530, doi:10.1029/2000JA000009.
- Romick, G. J. (1976), The detection and study of the visible spectrum of aurora and airglow, *SPIE Methods Atmos. Radiometry*, *91*, 63–70.
- Rostoker, G., J. C. Samson, F. Creutzberg, T. J. Hughes, D. R. McDiarmid, A. G. McNamara, A. Vallance Jones, D. D. Wallis, and L. L. Cogger (1995), Canopus – A ground-based instrument array for remote sensing the high latitude ionosphere during the ISTEP/GGS program, *Space Sci. Rev.*, *71*, 743–760.
- Sandholt, P. E., and C. J. Farrugia (2007), Poleward moving auroral forms (PMAFs) revisited: Responses of aurorae, plasma convection and Birkeland currents in the pre- and postnoon sectors under positive and negative IMF B_y conditions, *Ann. Geophys.*, *25*, 1629–1652.
- Sandholt, P. E., C. S. Deehr, A. Egeland, B. Lybekk, R. Viereck, and G. J. Romick (1986), Signatures in the dayside aurora of plasma transfer from the magnetosheath, *J. Geophys. Res.*, *91*(A9), 10,063–10,079, doi:10.1029/JA091iA09p10063.
- Sandholt, P. E., J. Moen, A. Rudland, D. Opsvik, W. F. Denig, and T. Hansen (1993), Auroral event sequences at the dayside polar cap boundary for positive and negative interplanetary magnetic field B_y , *J. Geophys. Res.*, *98*(A5), 7737–7755, doi:10.1029/92JA02256.
- Sandholt, P. E., et al. (1994), Cusp/cleft auroral activity in relation to solar wind dynamic pressure, interplanetary magnetic field B_z and B_y , *J. Geophys. Res.*, *99*, 17,323–17,342, doi:10.1029/94JA00679.
- Sandholt, P. E., C. J. Farrugia, J. Moen, Ø. Norberg, B. Lybekk, T. Sten, and T. Hansen (1998), A classification of dayside auroral forms and activities as a function of interplanetary magnetic field orientation, *J. Geophys. Res.*, *103*(A10), 23,325–23,345, doi:10.1029/98JA02156.
- Sandholt, P. E., C. J. Farrugia, S. W. H. Cowley, W. F. Denig, M. Lester, J. Moen, and B. Lybekk (1999), Capture of magnetosheath plasma by the magnetosphere during northward IMF, *Geophys. Res. Lett.*, *26*(18), 2833–2836, doi:10.1029/1999GL900600.
- Sandholt, P. E., H. C. Carlson, and A. Egeland (2002), *Dayside and Polar Cap Aurora*, 304 pp., Kluwer Acad., Dordrecht, Netherlands.

- Sandholt, P. E., B. Lybekk, A. Egeland, R. Nakamura, and T. Oguti (1989), Midday auroral breakup, *J. Geomagn. Geoelectr.*, *41*, 371–387.
- Sigernes, F., J. Moen, D. A. Lorentzen, C. S. Deehr, R. Smith, M. Øieroset, B. Lybekk, and J. Holtet (1996), SCIFER-Height measurements of the midmorning aurora, *Geophys. Res. Lett.*, *23*(14), 1889–1892, doi:10.1029/96GL01428.
- Sitar, R. J., J. B. Baker, C. R. Clauer, A. J. Ridley, J. A. Cumnock, V. O. Papitashvili, J. Spann, M. J. Brittnacher, and G. K. Parks (1998), Multi-instrument analysis of the ionospheric signatures of a hot flow anomaly occurring on July 24, 1996, *J. Geophys. Res.*, *103*, 23,357–23,372, doi:10.1029/98JA01916.
- Spann, J. F., M. Brittnacher, R. Elsen, G. A. Germany, and G. K. Parks (1998), Initial response and complex polar cap structures of the aurora in response to the January 10, 1997 magnetic cloud, *Geophys. Res. Lett.*, *25*, 2577–2580, doi:10.1029/98GL00647.
- Steele, D. P., D. J. McEwen, and G. G. Sivjee (1998), Ground-based optical observations from the north magnetic pole during the January 1997 magnetic cloud event, *Geophys. Res. Lett.*, *25*(14), 2573–2576, doi:10.1029/98GL01088.
- Strickland, D. J., J. R. Jasperse, and J. A. Whalen (1983), Dependence of auroral FUV emissions on the incident electron spectrum and neutral atmosphere, *J. Geophys. Res.*, *88*(A10), 8051–8062, doi:10.1029/JA088iA10p08051.
- Stringer, W. J. (1971), The relationship of auroral hydrogen emissions to auroral morphology, PhD thesis, Univ. of Alaska, Fairbanks.
- Su, Z., Q.-G. Zong, C. Yue, Y. Wang, H. Zhang, and H. Zheng (2011), Proton auroral intensification induced by interplanetary shock on 7 November 2004, *J. Geophys. Res.*, *116*, A08223, doi:10.1029/2010JA016239.
- Torr, M. R., et al. (1995), A far ultraviolet imager for the international solar-terrestrial physics mission, *Space Sci. Rev.*, *71*, 329–383.
- Thomsen, M. F., J. E. Borovsky, D. J. McComas, R. C. Elphic, and S. Maurice (1998), The magnetospheric response to the CME passage of January 10–11, 1997, as seen at geosynchronous orbit, *Geophys. Res. Lett.*, *25*(14), 2545–2548, doi:10.1029/98GL00514.
- Tsurutani, B. T., et al. (1998), The January 10, 1997, auroral hot spot, horseshoe aurora, and first substorm: A CME loop?, *Geophys. Res. Lett.*, *25*, 3047–3050, doi:10.1029/98GL01304.
- Tsurutani, B. T., et al. (2001a), Auroral zone dayside precipitation during magnetic storm initial phases, *J. Atmos. Sol. Terr. Phys.*, *63*, 513–522, doi:10.1016/S1364-6826(00)00161-9.
- Tsurutani, B. T., X.-Y. Zhou, V. M. Vasyliunas, G. Haerendel, J. K. Arballo, and G. S. Lakhina (2001b), Interplanetary shocks, magnetopause boundary layers and dayside auroras: The importance of a very small magnetospheric region, *Surv. Geophys.*, *22*(2), 101–130, doi:10.1023/A:1012952414384.
- Wüest, M. P., W. Lennartsson, and P. D. Craven (2002), Response of the dawn-side, high-altitude, high-latitude magnetosphere to the arrival of an interplanetary shockwave, *Adv. Space Res.*, *30*, 2189–2194, doi:10.1016/S0273-1177(02)80218-6.
- Vallance Jones, A., F. Creutzberg, R. L. Gattinger, and F. R. Harris (1982), Auroral studies with a chain of meridian-scanning photometers. I - Observations of proton and electron aurora in magnetospheric substorms, *J. Geophys. Res.*, *87*, 4489–4503, doi:10.1029/JA087iA06p04489.
- van Rhijn, P. J. (1921), *Pub. Astr. Lab. Groningen*, No. 31.
- Villante, U., P. Francia, S. Lepidi, M. De Lauretis, E. Pietropaolo, L. Cafarella, A. Meloni, A. J. Lazarus, R. P. Lepping, and F. Mariani (1998), Geomagnetic field variations at low and high latitude during the January 10–11, 1997 magnetic cloud, *Geophys. Res. Lett.*, *25*(14), 2593–2596, doi:10.1029/98GL00335.
- Vontrat-Reberac, A., J.-C. Cerisier, N. Sato, and M. Lester (2002), Noon ionospheric signatures of a sudden commencement following a solar wind pressure pulse, *Ann. Geophys.*, *20*, 639–645, doi:10.5194/angeo-20-639-2002.
- Vorobjev, V. G. (1977), Behavior of the dayside auroras after SC and SI, in *Structure of Magnetic-Ionospheric Disturbances* [in Russian], edited by G. A. Loginov et al., p. 126–132, Nauka, Leningrad, Russia.
- Vorobjev, V. G., O. I. Yagodkina, D. G. Sibeck, K. Liou, and C.-I. Meng (2001), Polar UVI observations of dayside auroral transient events, *J. Geophys. Res.*, *106*, 28,897–28,911, doi:10.1029/2000JA000396.
- Wüest, M., M. M. Huddleston, J. L. Burch, D. L. Dempsey, P. D. Craven, M. O. Chandler, J. F. Spann, W. K. Peterson, H. L. Collin, and W. Lennartsson (2000), Magnetospheric response to the arrival of the shock wave in front of the magnetic cloud of January 10, 1997, *Adv. Space Res.*, *25*(7–8), 1401–1404, doi:10.1016/S0273-1177(99)00651-1.
- Yang, Y. F., J. Y. Lu, J.-S. Wang, Z. Peng, Q. Qian, and Y. Xiao (2011), Different response of dayside auroras to increases in solar wind dynamic pressure, *J. Geophys. Res.*, *116*, A08314, doi:10.1029/2010JA016385.
- Zesta, E., H. J. Singer, D. Lummerzheim, C. T. Russell, L. R. Lyons, and M. J. Brittnacher (2000), The effect of the January 10, 1997, pressure pulse on the magnetosphere-ionosphere current system, in *Magnetospheric Current Systems*, *Geophys. Monogr. Ser.*, vol. 118, edited by S. Ohtani et al., p. 217, AGU, Washington, D. C.
- Zhang, Y., L. J. Paxton, T. J. Immel, H. U. Frey, and S. B. Mende (2003), Sudden solar wind dynamic pressure enhancements and dayside detached auroras: IMAGE and DMSP observations, *J. Geophys. Res.*, *108*(A4), 8001, doi:10.1029/2002JA009355.
- Zhang, Y., L. J. Paxton, and Y. Zheng (2008), Interplanetary shock induced ring current auroras, *J. Geophys. Res.*, *113*, A01212, doi:10.1029/2007JA012554.
- Zhou, X.-Y., and B. T. Tsurutani (1999), Rapid intensification and propagation of the dayside aurora: Large-scale interplanetary pressure pulses (fast shocks), *Geophys. Res. Lett.*, *26*, 1097–1100, doi:10.1029/1999GL900173.
- Zhou, X.-Y., and B. T. Tsurutani (2001), Interplanetary shock triggering of nightside geomagnetic activity: Substorms, pseudobreakups, and quiescent events, *J. Geophys. Res.*, *106*(A9), 18,957–18,967, doi:10.1029/2000JA003028.
- Zhou, X.-Y., R. J. Strangeway, P. C. Anderson, D. G. Sibeck, B. T. Tsurutani, G. Haerendel, H. U. Frey, and J. K. Arballo (2003), Shock aurora, FAST and DMSP observations, *J. Geophys. Res.*, *108*(A4), 8019, doi:10.1029/2002JA009701.
- Zhou, X.-Y., K. Fukui, H. C. Carlson, J. I. Moen, and R. J. Strangeway (2009), Shock aurora: Ground-based imager observations, *J. Geophys. Res.*, *114*, A12216, doi:10.1029/2009JA014186.

Erratum

In the originally published version of this article, an instance of text was incorrectly typeset. The following has since been corrected and this version may be considered the authoritative version of record.

A sentence in section 3 was updated to change the word “is” to “it”:

ZT99 used 72° MLAT for the dawnside calculation but specified that it was limited to 0600–1000 MLT.